



CRANFIELD UNIVERSITY

Josh Worwood

Development of a Low-Cost Stationary Plasma Thruster Testbed for
Use in Educational and Research Applications

SCHOOL OF AEROSPACE, TRANSPORT SYSTEMS &
MANUFACTURING

MSc ASTRONAUTICS & SPACE ENGINEERING
Academic Year: 2024 – 2025

Supervisor: Dr. Enric Grustan
August 2025

This report is submitted in partial fulfilment of the requirements for the degree of
MSc Astronautics & Space Engineering

© Cranfield University 2025. All rights reserved. No part of this publication may
be reproduced without the written permission of the copyright owner.

ABSTRACT

This report outlines the design and manufacture of a low-cost, laboratory-scale Stationary Plasma Thruster (SPT) test bed for educational and research use. With SPTs being increasingly adopted in both commercial constellations and deep-space missions, the project supports the development of UK technical expertise in electric propulsion by providing a manufacturable prototype accessible to graduate students.

The design was developed systematically, beginning with sub-kilowatt scaling laws to define geometry and operating parameters. Finite element analysis of the magnetic circuit was used to determine suitable radial-field distributions, which were translated into a manufacturable configuration through CAD modelling. Key components, including boron nitride channel inserts, EN1A steel magnetic structures, and custom wound electromagnets, were produced and assembled into two interchangeable short- and long-channel configurations.

The resulting prototype meets all aims presented, confirming that complex propulsion hardware can be realised within the scope of a master's thesis, whilst providing a valuable platform for future research and training at Cranfield University.

KEYWORDS

Hall Effect Thruster (HET), Stationary Plasma Thruster (SPT), Electric Propulsion (EP), Argon Propellant, Magnetic Circuit Design, Thruster Prototyping, Sub-Kilowatt Thruster, Plasma Acceleration

ACKNOWLEDGEMENTS

I would like to express my sincere gratitude to my supervisor, Dr. Enric Grustan, for his guidance, support, and encouragement throughout this project. His willingness to support an experimental and ambitious undertaking such as this, when many might not, was invaluable to both the development of the thruster and my growth as an engineer. I would also like to thank Cranfield University for providing the academic environment and facilities that made this work possible.

Disclaimer:

Generative artificial intelligence (ChatGPT and Writefull) has been used to improve the readability and structure of this report. All technical content, including calculations, data, analysis, and designs, is entirely the work of the author.

Contents

ABSTRACT	i
ACKNOWLEDGEMENTS	ii
LIST OF ABBREVIATIONS	ix
	ix
1 Introduction	1
1.1 Overview	1
1.2 Fundamental Performance Parameters	1
1.3 Classification of Electric Propulsion Systems	2
1.4 The Development and Current State of EP	3
1.5 Project Motivation and Objectives	4
2 HET Operating Principals	5
2.1 Electron Confinement and Hall Current	6
2.2 Ion Acceleration, Thrust, and Exhaust Velocity	9
2.3 Efficiency Considerations	10
2.3.1 Ionisation and Propellant Utilisation	10
2.3.2 Electron Transport and Anomalous Diffusion	11
2.3.3 Plume Divergence	12
2.3.4 Wall Interactions and Energy Losses	13
2.3.5 Overall Effective Efficiency	14
3 Thruster Design	16
3.1 Aims and Requirements	16
3.1.1 Aims	16
3.1.2 Requirements	17
3.2 Initial Scaling	18
3.2.1 Methodology	18
3.3 Magnetic Circuit Design	24
3.3.1 Coil Layout Subsection	24
3.3.2 2D Model	26
3.3.3 Simulation Setup	27
3.3.4 Short Configuration Results	28
3.3.5 Long Configuration Results	33
3.4 Detailed Design	36

3.4.1	Mechanical Design and CAD Modelling	37
3.4.2	Magnetic Material Substitution	42
3.4.3	Propellant Feed System	43
3.4.4	Cathode Integration	45
3.4.5	Electrical System and Wiring	47
4	Thruster Assembly	49
4.1	Coil Winder	49
4.1.1	Coil Consistency	52
4.2	Boron Nitride Inserts	53
4.3	Machined Parts	55
4.4	Thruster Assembly	56
5	Conclusion	60
5.1	Cost Breakdown	60
5.2	Future Work	62
5.3	Final Word	63
A	Executive Summary: Development of a Low-Cost Stationary Plasma Thruster Testbed for Use in Educational and Research Applications	67
B	Appendix B	71
B.1	Scaling Law Dataset	71
B.2	SCCM Conversion Script - Matlab	72
B.3	Larmor Radius - Matlab	73
B.4	Coil Winder Arduino Sketch	74

List of Figures

1	Schematic of a typical Stationary Plasma Thruster showing the anode, dielectric discharge channel, the cathode, radial magnetic field, and axial electric field.	6
2	Schematic representation of the cylindrical coordinate system in a Hall thruster, showing the axial electric field (E_z), radial magnetic field (B_r), and the resulting azimuthal electron drift velocity (v_E) that constitutes the Hall current.	8
3	Comparison of unshielded (left) and magnetically shielded (right) Stationary Plasma Thruster (SPT) configurations. In both cases, the axial electric field (E_z) and its components relative to the magnetic field (E_\perp , perpendicular; E_\parallel , parallel) are shown. The lower graphs show the plasma potential (ϕ) and electron temperature of each configuration. Diagram adapted from [1]	13
4	Scaling of anode power with the geometric–electrical parameter $U_d d^2$ for sub-kilowatt Hall thrusters. Black points indicate reference thrusters, the dashed line shows the empirical fit $P_d = 633 U_d d^2$, and the shaded region denotes the 95% prediction band. The present design is marked in red.	19
5	Relationship between mean channel diameter (d) and channel width (h) for Hall thrusters in the reference dataset. The dashed line shows the scaling law $h = 0.242 d$, with the shaded region indicating the 95% prediction band. Black points represent reference thrusters, while the red marker denotes the present design.	20
6	Scaling of anode mass flow rate with the geometric parameter $h d$ for sub-kilowatt Hall thrusters. Black points represent reference devices, the dashed line shows the empirical correlation $\dot{m}_a = 0.003 h d$, and the shaded region denotes the 95% prediction band. The present design is indicated in red.	21
7	Scaling of thrust with the parameter $\dot{m}_a U_d^{0.5}$ for sub-kilowatt Hall thrusters. Experimental thrusters are shown as black points, the dashed line indicates the empirical correlation $T = 892.7 \dot{m}_a U_d^{0.5}$, and the shaded region represents the 95% prediction interval. The present design point is shown in red.	22
8	2D parametric model of the thruster magnetic circuit in Ansys Maxwell, showing magnetic cores (grey), coils (orange), and discharge channel (white).	27

9	Magnetic vector potential distribution and flux lines for the short configuration.	31
10	Magnetic flux density distribution for the short configuration.	32
11	Axial magnetic field strength along the channel centreline for the short configuration at different coil currents.	33
12	Magnetic vector potential distribution and flux lines for the long configuration.	34
13	Magnetic flux density distribution for the long configuration.	35
14	Axial magnetic field strength along the discharge channel centreline for the long configuration at different coil currents.	36
15	Isometric CAD view of the boron nitride discharge channel insert. .	38
16	Top-down CAD view of the boron nitride discharge channel insert.	38
17	CAD model of the short configuration, showing discharge channel, coil regions, and supporting magnetic cores.	39
18	CAD model of the long configuration, showing extended discharge channel and increased coil winding allowance.	40
19	Exploded CAD view of the thruster assembly, showing channel insert, coils, magnetic circuit, and supporting structure.	41
20	3D printed mock-ups used to validate assembly, fit, and robustness of the CAD model.	42
21	Schematic of the propellant feed system, showing argon supply, mass flow control, vacuum chamber interface, electrical isolation, and anode connection.	44
22	CAD model of the anode and propellant feed interface.	45
23	Prospective cathode elements: 21 W automotive bulbs and holders, to be repurposed as filament cathodes after removal of the glass housings.	46
24	Simplified wiring schematic of the thruster showing independent supplies for the discharge circuit, electromagnet coils, and cathode filaments. All circuits share a common ground at the vacuum chamber, with HV and LV feedthroughs segregated.	48
25	Steel coil cores prior to winding.	49
26	Custom-built coil winder with annotated components.	50
27	Close-up of the winding process showing wire guide and coil core.	51
28	Completed short (right) and long (left) coils after winding and being wrapped in polyimide tape.	52

29	Boron nitride discharge channel inserts for the short (left) and long (right) thruster configurations, as received from the supplier.	54
30	Close-up of the boron nitride insert showing minor edge rounding and localised crumbling at sharp corners after test fitting.	54
31	Machined EN1A steel components for the thruster magnetic circuit including the pole pieces (left) and the baseplate (right).	56
32	Thruster during mid-assembly showing the coils and BN inserts installed on the magnetic base.	57
33	Completed thruster assembly in the short-channel configuration. .	58
34	Completed thruster assembly in the long-channel configuration. . .	59

List of Tables

1	Typical performance parameters for representative chemical and electric propulsion thruster types. The values are indicative ranges for specific impulse, thrust, and common propellants [1].	3
2	Summary of design parameters derived from Lee et al.'s xenon scaling laws, adapted for argon, and final values selected for the design.	24
3	2D Model Fixed Input Parameters	26
4	Summary of short configuration parameters used in magnetic circuit modelling.	30
5	Summary of long configuration parameters used in magnetic circuit modelling.	34
6	Measured resistances of short and long coils used to assess winding consistency.	52
7	Cost breakdown of the thruster and ancillary systems. *note this value excludes vacuum chamber costs	61
8	Dataset of Hall Effect Thrusters primarily in the sub-kilowatt range used to establish the scaling law applied in this study. Columns list: P (input power, W), U_d (discharge voltage, V), d (mean channel diameter, mm), h (channel width, mm), L (channel length, mm), \dot{m}_p (propellant mass flow rate, mg/s), T (thrust, mN), and I_{sp} (specific impulse, s). [28]	71

LIST OF ABBREVIATIONS

AEDT Ansys Electronics Desktop.

EP Electric Propulsion.

FEA Finite Element Analysis.

HET Hall Effect Thruster.

I_{sp} Specific Impulse.

LEO Low Earth Orbit.

MPD Magnetoplasdynamic.

PPT Pulsed Plasma Thruster.

SPT Stationary Plasma Thruster.

TAL Thruster with Anode Layer.

1 Introduction

1.1 Overview

Spacecraft propulsion is fundamental to almost every aspect of satellite and mission design. A wide range of propulsion technologies are available, each with different advantages, limitations, and mission suitability. To select the most appropriate system for a given application, it is essential to compare these technologies using a common set of fundamental performance relations. Establishing these parameters first ensures a fair comparison between different propulsion concepts.

1.2 Fundamental Performance Parameters

One of the most fundamental relationships is the Tsiolkovsky rocket equation, shown in Eq. (1.1), which relates the total achievable change in spacecraft velocity to the thruster's specific impulse and the ratio of initial to final mass

$$\Delta V = g_0 I_{sp} \ln \frac{m_0}{m_1} \quad (1.1)$$

Here, ΔV is the total change in velocity, g_0 is the standard gravitational acceleration, I_{sp} is the specific impulse, and m_0 and m_1 are the initial and final spacecraft masses respectively. The specific impulse is defined as the thrust produced per unit of propellant weight flow rate, providing a direct measure of how effectively a propulsion system uses its propellant. Higher specific impulse values indicate that a given amount of propellant can deliver a greater total impulse, enabling the same ΔV to be achieved with less propellant.

The thrust generated by a propulsion system can generally be expressed as

$$F = \dot{m} v_e + (p_e - p_0) A_e \quad (1.2)$$

Here, v_e is the exhaust velocity, p_e is the exhaust pressure, p_0 is the ambient pressure, and A_e is the nozzle exit area. For in-space operations, p_e is typically very close to p_0 allowing the pressure term to be neglected. The thrust therefore reduces to:

$$F = \dot{m}v_e \quad (1.3)$$

This expression links directly with Eq. (1.4), as exhaust velocity is related to the specific impulse by

$$v_e = I_{sp}g_0 = \frac{F}{\dot{m}} \quad (1.4)$$

Since g_0 is fixed, values of specific impulse are often reported either in seconds or equivalently in terms of exhaust velocity in metres per second.

For chemical rockets, the maximum exhaust velocity is fundamentally limited by the chemical potential energy of the propellants, with further losses during the conversion of that energy into kinetic energy. In contrast, Electric Propulsion (EP) systems are not bound by chemical energy release and can achieve much higher exhaust velocities and therefore higher efficiencies. For spacecraft, this capability can extend mission lifetimes or reduce overall mass by lowering propellant requirements. The trade-off is that EP thrusters typically generate very low thrust, so manoeuvres take significantly longer than with chemical propulsion.

1.3 Classification of Electric Propulsion Systems

EP systems are generally classified into three main categories according to the mechanism by which they accelerate the propellant:

- **Electrothermal:** These thrusters apply heat electrically to the propellant prior to expansion through a nozzle (e.g. resistojets, arcjets)
- **Electrostatic:** These thrusters use electrostatic fields to directly accelerate charged particles (e.g. ion thrusters)
- **Electromagnetic:** These thrusters use the interaction of electric and magnetic fields within a plasma to accelerate the propellant (e.g. Magnetoplasma dynamic (MPD) thrusters)

As shown in Table 1, these categories span a broad range of performance. While EP thrusters achieve much higher Specific Impulse (I_{sp}) than chemical systems, they typically produce far lower thrust.

Thruster	Specific Impulse (sec)	Thrust	Propellant
Cold Gas	25 - 75	0.1 - 100 N	Various
Solid Chemical	250 - 304	10^7 N	Various
Liquid Chemical (monopropellant)	150 - 235	1 - 500 N	N_2H_4 , H_2O_2
Liquid Chemical (bipropellant)	274 - 467	10^7 N	Various
Resistojet	100 - 300	0.5 - 6000 mN	N_2H_4
Arcjet	130 - 600	50 - 6800 mN	N_2H_4
Ion Thruster	2500 - 4000	0.1 - 750 mN	Xe , Kr
HET	1500 - 3000	0.1 - 2000 mN	Xe , Kr
PPT	850 - 1200	0.05 - 10 mN	Teflon
MPD	200 - 3200	0.1 - 2000 mN	H_2 , Li , Ar , Xe

Table 1: Typical performance parameters for representative chemical and electric propulsion thruster types. The values are indicative ranges for specific impulse, thrust, and common propellants [1].

1.4 The Development and Current State of EP

Early investigations into EP focused predominantly on four types: ion thrusters, Pulsed Plasma Thrusters (PPTs), resistojets, and Hall Effect Thrusters (HETs) [2]. The first successful in-orbit demonstration was a PPT flown in 1964 aboard the Soviet Zond-2 spacecraft [3], and by the late 1960s ion thrusters and resistojets had also achieved operational success, establishing EP as a viable alternative to chemical propulsion for attitude control. During this same period, significant effort in the USSR was devoted to the development of the HET [4]. Its combination of relatively high thrust and good efficiency sustained interest throughout the decade and led to its first successful flight in 1971 aboard the Meteor 1-10 weather satellite [5].

Initial use of HETs was largely confined to Soviet spacecraft. Their migration to Western markets accelerated in the 1990s, aided by the collapse of the Soviet Union. This decade also marked a broader shift in electric propulsion, as usage expanded from predominantly state-operated spacecraft to increasing adoption in commercial missions. Improvements in lifetime, efficiency, reliability, and cost, combined with performance advantages over arcjets, which at the time dominated geostationary satellite electric propulsion, made HETs the preferred choice for

station-keeping and later orbit-raising.

Since then, HETs have expanded into a broad range of spacecraft applications. Their dominance in the satellite EP market has been reinforced by recent demand from large Low Earth Orbit (LEO) constellations such as Starlink and OneWeb [6, 7], where they are valued for their balance of thrust, specific impulse, operational lifetime, and cost.

1.5 Project Motivation and Objectives

The growing role of HETs in commercial constellations and deep-space missions [8] highlights their strategic value to the global space sector. Building the capability to design, manufacture, and test HETs within the UK and Europe is essential for strengthening domestic expertise and reducing reliance on external suppliers. Such capability ensures that regional suppliers remain competitive and able to provide critical propulsion technology for future missions.

This project aims to contribute to that goal through the design and manufacture of an in-house modular HET for laboratory use. The work has two primary objectives: first, to provide a low-cost, practical platform for developing hands-on experience in HET operation, diagnostics, and performance evaluation; and second, to facilitate research into alternative propellants, supporting the diversification of propulsion options for future space missions.

2 HET Operating Principals

The Hall thruster is generally considered an electrostatic device, because the primary mechanism of propellant acceleration is the axial electric field within the discharge channel. Some sources categorise HETs as electromagnetic devices due to the role of the radial magnetic field in electron confinement and Hall current generation. However, following the classification definition outlined earlier in this document, we will treat the HET as an electrostatic device.

The basic geometry of a conventional HET consists of a coaxial discharge channel, a cathode located near the exit of the channel, an anode at the base of the channel, and a set of electromagnetic coils and ferromagnetic circuits that shape the magnetic field. The radial magnetic field strength is concentrated near the channel exit, while the axial electric field extends through the channel. Electrons emitted from the cathode attempt to move axially towards the anode under the influence of the electric field. However, the radial magnetic field prevents them from moving directly to the anode. Instead, the electrons spiral with tight Larmor orbits around the magnetic field lines and undergo an azimuthal $\mathbf{E} \times \mathbf{B}$ drift. This collective azimuthal motion constitutes the Hall current, which provides the energetic electrons necessary to sustain ionisation of the propellant and, by impeding cross-field transport, helps maintain the axial potential drop required for ion acceleration.

Within this general architecture, two widely used HET configurations have emerged: SPTs and Thrusters with Anode Layer (TALs). The SPT employs a relatively long discharge channel lined with a dielectric material, whereas the TAL features a shorter, electrically conductive channel with the acceleration zone positioned closer to the anode. Although TALs are theorised to offer a higher specific impulse than SPTs, they typically produce lower thrust, impose greater thermal loads on the anode, and exhibit lower discharge stability [9, 10]. TALs also have a more limited operational heritage, the experimental database is comparatively sparse. By contrast, SPTs have seen widespread adoption in both commercial and institutional programmes and are now the dominant configuration in modern HET design. This project will focus on the SPT configuration.

A schematic for a typical SPT is shown in Fig. 1, illustrating the key functional components and field configurations.

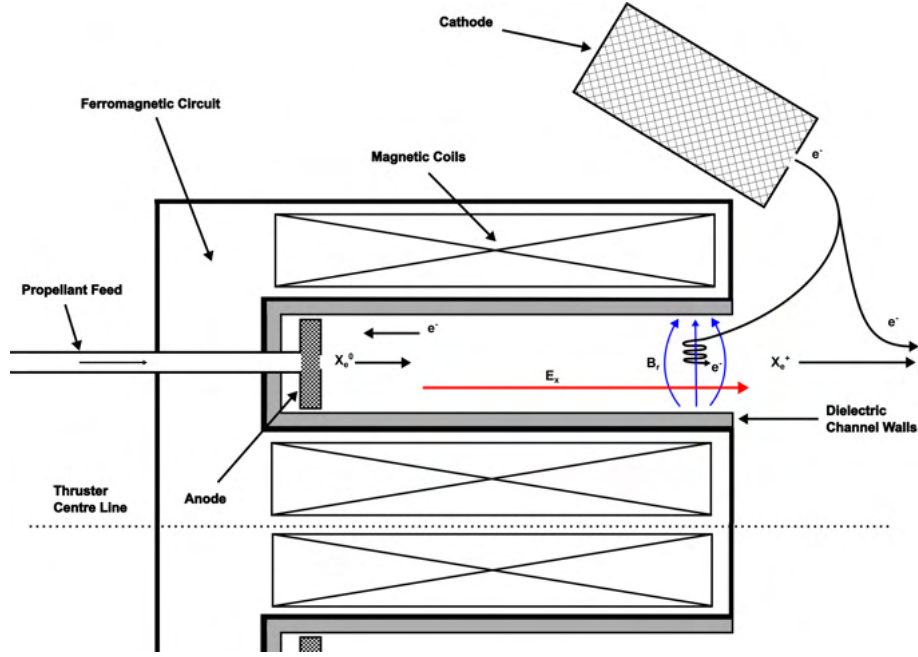


Figure 1: Schematic of a typical Stationary Plasma Thruster showing the anode, dielectric discharge channel, the cathode, radial magnetic field, and axial electric field.

Recent developments have focused on magnetic shielding, in which the magnetic field shape is tailored to deflect high-energy ions away from the channel walls. This greatly reduces wall erosion, extends operational lifetime, and allows higher power operation. As a result, magnetically shielded designs have become increasingly important in modern EP applications, particularly for deep-space missions where service life is critical.

The next section explores the underlying physics of HET operation, examining how magnetic confinement, electron dynamics, and ion acceleration mechanisms determine overall performance. These principles form the foundation for the design and scaling analyses presented later in this work.

2.1 Electron Confinement and Hall Current

One of the defining features of a Hall thruster is the radial magnetic field applied across the discharge channel. When a charged particle enters a magnetic field, it exhibits circular motion about the field lines known as Larmor precession. The radius of this orbit depends on the particle's velocity, charge, and the strength of the magnetic field. In a Hall thruster, electrons emitted from the cathode attempt to move axially towards the anode under the influence of the applied axial electric

field, but their motion is strongly constrained by the magnetic field, which forces them into tight orbits.

The electron Larmor radius is given by

$$r_e = \frac{v_{th}}{\omega_c} = \frac{m_e}{eB} \sqrt{\frac{8kT_e}{\pi m_e}} = \frac{1}{B} \sqrt{\frac{8}{\pi} \frac{m_e}{e} T_{eV}} \ll L \quad (2.1)$$

where m_e is the electron mass, B the magnetic field strength, T_{eV} the electron temperature (in eV), and $\omega_c = eB/m_e$ is the electron cyclotron frequency. In a well-designed Hall thruster, r_e (the electron Larmor radius) is much smaller than the magnetised plasma depth, L , ensuring that electrons complete many orbits and remain effectively magnetised.

In contrast, ions have a much larger Larmor radius:

$$r_i = \frac{v_i}{\omega_{ci}} = \frac{M}{eB} \sqrt{\frac{2eV_b}{M}} = \frac{1}{B} \sqrt{\frac{2M}{e}} V_b \gg L \quad (2.2)$$

with M the ion mass, V_b the effective beam voltage (closely related to but slightly lower than the applied discharge voltage V_d), and $\omega_{ci} = eB/M$. Since $r_i \gg L$, the ions are effectively unmagnetised and are accelerated axially by the electric field without being significantly influenced by the magnetic field.

For illustration, in a typical SPT operating with xenon at $B \approx 200G$, an electron at 20 eV has a Larmor radius on the order of 0.1 mm, whereas an ion at 300 V has a Larmor radius exceeding 1 m.

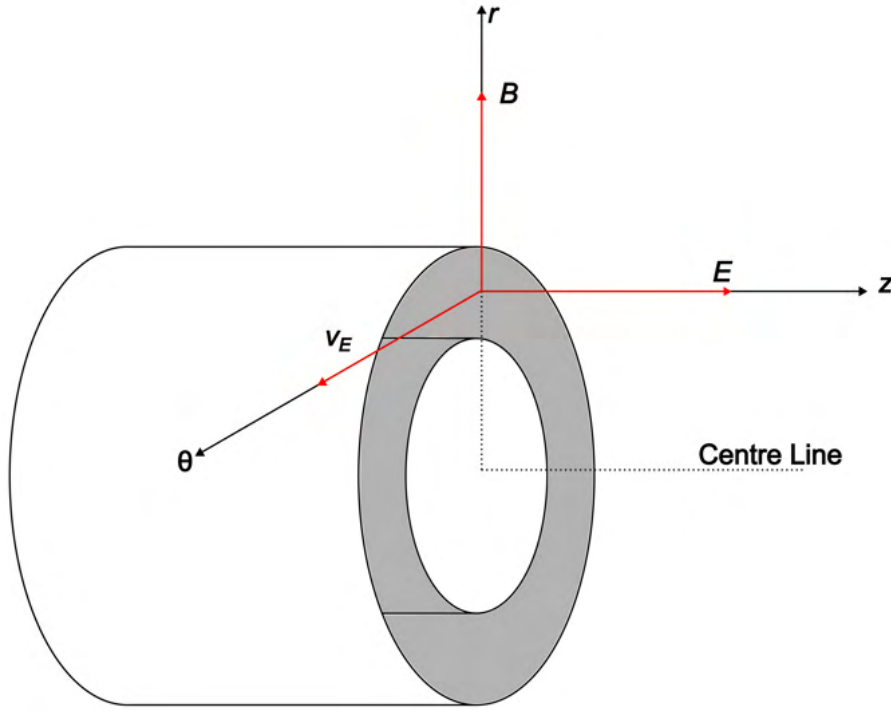


Figure 2: Schematic representation of the cylindrical coordinate system in a Hall thruster, showing the axial electric field (E_z), radial magnetic field (B_r), and the resulting azimuthal electron drift velocity (v_E) that constitutes the Hall current.

As illustrated in Fig. 2, the position of an axial electric field and a radial magnetic field produces an azimuthal $\mathbf{E} \times \mathbf{B}$ drift velocity which can be approximated using

$$v_E = \frac{|\mathbf{E} \times \mathbf{B}|}{B^2} \approx \frac{E_z}{B_r} \quad (2.3)$$

This drift is the characteristic $\mathbf{E} \times \mathbf{B}$ motion of electrons. Since the bulk of the electron population undergoes this drift, their collective motion forms a strong azimuthal current encircling the discharge channel, known as the Hall current. Although a full derivation lies beyond the scope of this work, it can be shown that the Hall current is related to the ion current according to

$$I_H \approx \frac{I_i}{2\pi R B} \sqrt{\frac{M V_d}{2e}} \quad (2.4)$$

where I_i is the total ion current, R is the average radius of the plasma channel, and e is the elementary charge.

The Hall current sustains the plasma discharge and couples electron confinement directly to ion acceleration. This leads to an approximate expression for the thrust

$$T = I_H B \approx I_i \sqrt{\frac{M V_d}{2e}} \quad (2.5)$$

These relations are not intended as precise design tools but rather as a means to illustrate the link between geometry, discharge conditions, and performance. Specifically, they show how the discharge voltage, magnetic field, channel geometry, and ion mass collectively determine both the magnitude of the Hall current and the thrust that results from it.

2.2 Ion Acceleration, Thrust, and Exhaust Velocity

Having established how the applied magnetic field confines electrons and sustains the discharge through the Hall current, we now turn to the behaviour of the ions. Neutral propellant atoms, injected via the anode, are ionised primarily through electron impacts in the near-exit region of the discharge channel, where the axial electric field is strongest. Once created, these ions are accelerated axially across an effective potential drop, which is often approximated as the discharge voltage. In reality, the actual potential seen by the ions is somewhat lower due to losses and non-ideal effects.

The acceleration of ions in a Hall thruster can be understood by equating the electrical potential energy gained by a single charged ion to its kinetic energy at the channel exit. This gives the energy balance

$$\frac{1}{2} M_i v_i^2 \approx e V_d \quad (2.6)$$

Where M_i is the ion mass, v_i is the exhaust velocity, e is the elementary charge, and V_d is the discharge voltage. This simple relation assumes that the ion is accelerated primarily by the axial electric field and that the energy losses to other mechanisms are small.

Rearranging yields an expression for the ion exhaust velocity

$$v_i \approx \sqrt{\frac{2e V_d}{M_i}} \quad (2.7)$$

Which shows directly how the ion mass and discharge voltage set the characteristic speed of the exhaust. This velocity can then be used in the equation for thrust in a vacuum, Eq. (1.3), derived in Chapter 1 to give

$$F \approx \dot{m}v_i \quad (2.8)$$

where \dot{m} is the propellant mass flow rate. From the exhaust velocity, the specific impulse can also be found

$$I_{sp} = \frac{v_i}{g_0} \quad (2.9)$$

These expressions connect the acceleration physics inside the channel directly with the performance parameters already introduced in Chapter 1.

For a thruster using xenon as a propellant at a discharge voltage of 300 V, this simple model predicts an exhaust velocity of about 20 km/s, corresponding to a specific impulse near 2000 s. These values represent the theoretical performance ignoring losses, in reality most thrusters achieve a somewhat lower specific impulse between 1000 - 1500 s [11, 12].

2.3 Efficiency Considerations

The ideal thrust and exhaust velocity relations presented earlier assume that all of the discharge power is converted into directed ion kinetic energy. In practice, several mechanisms reduce efficiency. These can be grouped into ionisation losses, electron transport losses, plume divergence, and wall interactions.

2.3.1 Ionisation and Propellant Utilisation

For Hall thrusters, the propellant utilisation efficiency is an important efficiency term, which describes the fraction of injected neutral atoms that are successfully ionised within the discharge channel. Neutrals that escape without being ionised do not contribute to thrust, meaning that a portion of the electrical input power is effectively wasted, as it sustains the discharge without producing useful accelerated ions.

The likelihood of ionisation depends upon the ionisation mean free path, λ_i , which is the average distance a neutral propellant atom travels before undergoing an

ionising collision with an electron. It can be expressed as

$$\lambda_i = \frac{v_n}{n_e \langle \sigma_i v_e \rangle} \quad (2.10)$$

where v_n is the neutral particle velocity, n_e is the electron number density, and $\langle \sigma_i v_e \rangle$ is the velocity averaged ionisation cross-section [1]. From this it is clear λ_i decreases with higher electron density or ionisation cross-section, and increases with faster-moving neutral atoms.

For efficient operation, the plasma length L should be significantly larger than λ_i , ensuring that most neutral atoms undergo at least one ionising collision before exiting the channel. A common expression for the propellant utilisation efficiency is

$$\eta_p = 1 - e^{-\frac{L}{\lambda_i}} \quad (2.11)$$

This shows that as L/λ_i increases, η_p approaches unity. In practice, designs aim for $L \gg \lambda_i$, ensuring high utilisation, whilst balancing against the increased wall interactions that come with longer channels.

2.3.2 Electron Transport and Anomalous Diffusion

In an ideal Hall thruster, the electrons would be fully magnetised, with their motion restricted to tight Larmor orbits. Under such conditions, cross-field transport toward the anode would occur only through classical collisions with neutral atoms. However, measured electron currents to the anode are often one to two orders of magnitude higher than those predicted by classical collision theory [13, 14]. This discrepancy is attributed to anomalous electron transport.

The strength of electron confinement is characterised by the Hall parameter

$$\Omega_e = \frac{\omega_c}{\nu} \quad (2.12)$$

where $\omega_e = eB/m_e$ is the electron cyclotron frequency and ν is the effective collision frequency. In a well designed thruster, $\Omega_e^2 \gg 1$, meaning electrons should be strongly magnetised [1]. In practice, however, fluctuations in plasma density

and electric field create effective scattering processes that increase ν , thereby lowering the confinement and enhancing cross-field diffusion.

The additional current drawn by this transport does not directly contribute to ion acceleration but still dissipates input power. As a result, anomalous transport represents one of the dominant loss mechanisms in Hall thrusters. Models for this behaviour often use Bohm diffusion scaling, in which the effective electron mobility across magnetic field lines is proportional to $1/B$. Although widely used, Bohm diffusion should be seen as an empirical approximation rather than a rigorous description of the underlying turbulence responsible for anomalous transport [15, 16].

Experimental and numerical studies continue to refine the understanding of anomalous transport. From a performance perspective, however, its effect is to reduce overall efficiency by diverting a fraction of the discharge current away from propellant ionisation and acceleration.

2.3.3 Plume Divergence

In addition to electron transport losses, Hall thruster efficiency is also affected by plume divergence. The ions are not accelerated perfectly along the thruster axis but instead leave the channel with a spread in their velocity vectors. The resulting plume is characterised by a finite divergence angle, reflecting the spread of ion velocities away from the axis. As a result, only the axial component of the ion momentum contributes to useful thrust, while the radial component is effectively wasted.

The thrust efficiency associated with plume divergence is expressed as

$$\eta_d = \frac{\langle v_z \rangle}{\langle v \rangle} \quad (2.13)$$

where $\langle v_z \rangle$ is the average axial ion velocity and $\langle v \rangle$ the average total ion velocity.

Typical Hall thrusters exhibit beam divergence half-angles of 20° - 40° [1, 17]. Minimising this divergence is an important aspect of thruster design, with optimisation of the magnetic field near the channel exit shown to improve collimation and enhance overall efficiency [18].

2.3.4 Wall Interactions and Energy Losses

In SPTs, a portion of the accelerated ions inevitably collide with the dielectric channel walls. These interactions reduce efficiency in two ways: first, by removing ion momentum that would otherwise contribute to thrust, and second, by introducing additional loss mechanisms within the plasma. Energetic ions striking the walls can erode material through processes such as sputtering and charge exchange [19], gradually altering the channel geometry and limiting thruster lifetime. Wall interactions also release secondary electrons, which enhance cross-field electron transport and increase anomalous diffusion. This feedback not only reduces confinement but can destabilise the discharge under certain operating conditions.

To mitigate these effects, modern SPTs increasingly employ magnetic shielding, in which the magnetic field topology is reshaped to minimise the flux of energetic ions reaching the walls [20, 1].

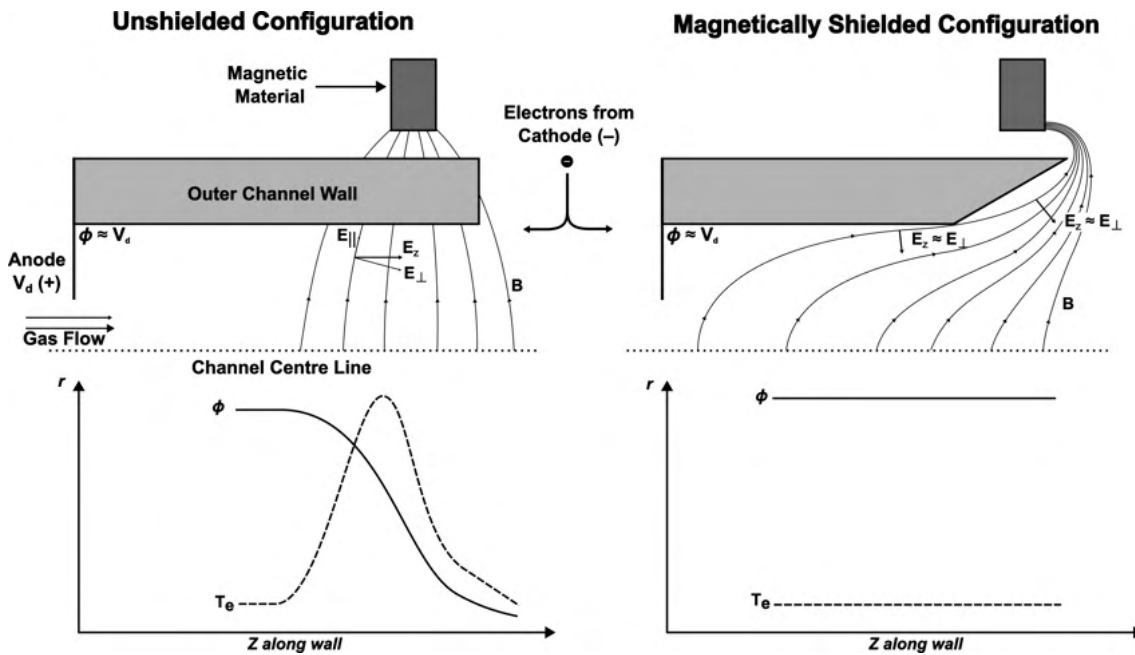


Figure 3: Comparison of unshielded (left) and magnetically shielded (right) SPT configurations. In both cases, the axial electric field (E_z) and its components relative to the magnetic field (E_{\perp} , perpendicular; E_{\parallel} , parallel) are shown. The lower graphs show the plasma potential (ϕ) and electron temperature of each configuration. Diagram adapted from [1]

In the unshielded configuration, the electric field near the channel wall includes a significant parallel component E_{\parallel} , which drives ions into the dielectric surface. By contrast, the shielded configuration reshapes the magnetic topology such that $E_z \approx E_{\perp}$ at the walls, effectively eliminating E_{\parallel} . This prevents ions from being accelerated into the walls and instead confines them to the axial direction. The lower plots highlight the impact on plasma properties: in the unshielded case, steep gradients in plasma potential (ϕ) and electron temperature (T_e) exist near the wall, whereas shielding flattens these profiles, reducing energy losses and enhancing confinement.

These improvements account for the extended lifetimes and enhanced performance of shielded thrusters [21, 22]. Nonetheless, implementing an effective shielded configuration requires extensive optimisation of the magnetic circuit, adding significant design and manufacturing challenges. For the purposes of this project, this placed shielding beyond the scope of the initial design. Therefore, a conventional unshielded configuration has been adopted, with the expectation that future iterations could incorporate shielding once a baseline design is established.

2.3.5 Overall Effective Efficiency

The combined effects of incomplete ionisation, anomalous electron transport, plume divergence, and wall interactions mean that only a fraction of the electrical input power is converted into useful ion kinetic energy. While these mechanisms can be considered separately in theory, isolating their individual contributions in practice is challenging, since they are strongly coupled. For this reason, Hall thruster performance is often described using compact efficiency metrics that capture the overall effect.

The most general is the total efficiency, which relates thrust, propellant flow, and discharge power:

$$\eta_T = \frac{T^2}{2\dot{m}_p P_{in}} \quad (2.14)$$

The total efficiency encompasses all loss mechanisms, including the additional power consumed by the cathode and magnets. To focus specifically on the plasma production and ion acceleration processes within the discharge channel, it is common to use the anode efficiency, defined as

$$\eta_a = \frac{1}{2} \frac{T^2}{\dot{m}_a P_d} \quad (2.15)$$

where \dot{m}_a is the anode propellant flow rate and P_d the discharge power. The anode efficiency is related to the total efficiency through

$$\eta_a = \frac{\eta_T}{\eta_o \eta_c} \quad (2.16)$$

with

$$\eta_o = \frac{P_d}{P_{in}}, \quad \eta_c = \frac{\dot{m}_a}{\dot{m}_p} \quad (2.17)$$

Here η_o is the power utilisation efficiency, representing the fraction of total input power supplied to the discharge, and η_c is the propellant utilisation factor, representing the fraction of propellant injected through the anode.

Since η_T includes the penalties from cathode power draw, magnet losses, and non-anode propellant flows, it is always lower than η_a . In practice, η_a values of 50 – 70% are common in state-of-the-art devices [23, 24, 25], reflecting how effectively the discharge channel itself converts electrical power and propellant into directed ion energy. By contrast, η_T values typically fall in the 30 – 60% range [26, 25, 27]

In general, anode efficiency is the metric of choice for thruster-level analysis and optimisation, as it isolates the plasma production and ion acceleration mechanisms inside the channel. Total efficiency, on the other hand, is more relevant for system and mission level assessments, where auxiliary subsystems must also be considered when evaluating propulsion performance.

In summary, the operating principles and efficiency considerations outlined in this chapter provide the physical framework needed to understand Hall thruster behaviour. The interplay between electron confinement, ion acceleration, and loss mechanisms defines the performance envelope of these devices and highlights the trade-offs that must be managed in practical designs. With this foundation established, the following chapter presents the design of the Stationary Plasma Thruster test bed developed in this project.

3 Thruster Design

With the physical principles established, the focus now shifts from theory to application. This chapter details the design of the Stationary Plasma Thruster test bed developed in this project, showing how the concepts introduced in Chapter 2 were translated into a practical laboratory device.

The design process began with the definition of aims and operational requirements, which set the boundaries for performance, cost, and complexity. Initial sizing was then carried out using established sub-kilowatt SPT scaling laws to determine the baseline geometry and power envelope. The magnetic circuit was subsequently modelled in Ansys Maxwell to produce the desired radial field profile, before progressing to the detailed CAD design of the discharge channel, anode, coils, and support structures.

Together, these stages form a coherent workflow that links theoretical understanding to engineering practice, culminating in a manufacturable thruster configuration suitable for experimental use.

3.1 Aims and Requirements

Defining aims and requirements is a central part of the engineering design process. The aims provide the broader purpose and direction of the project, while the requirements translate these objectives into concrete, measurable criteria against which the success of the final design can be assessed. Together, they form the framework that guided the design of the Stationary Plasma Thruster (SPT) test bed.

3.1.1 Aims

The overarching aims of this project were:

- To develop a low-cost, accessible Hall thruster test bed that demonstrates the fundamental operating principles of an SPT
- To create a platform suitable for training and educational use, enabling students to gain hands-on experience with electric propulsion
- To provide a reusable foundation for future research activities at Cranfield University, supporting further investigations into scaling, efficiency improve-

ments, thruster characterisation, and alternative propellant concepts.

3.1.2 Requirements

To achieve these aims, the thruster was required to meet the following criteria:

- The thruster shall operate at a maximum power of 150 W
- The thruster shall operate at discharge voltages up to 300 V
- The total cost of the thruster (excluding external operating equipment) shall be kept under £1000
- The thruster shall be capable of operating in two interchangeable channel length configurations
- The thruster shall be designed to operate using argon as the primary propellant, with provisions for alternative gases
- The thruster shall be sufficiently robust to withstand repeated assembly, disassembly, and handling for educational use

The maximum power was capped at 150 W, reflecting both the limitations of the laboratory vacuum facility and the project budget. The discharge voltage ceiling of 300 V was defined by the constraints of the available laboratory power supplies. The total cost cap of £1000 was imposed as a project budgetary requirement, reflecting the emphasis on affordability and accessibility for continued academic use. The inclusion of interchangeable channel lengths was intended to provide flexibility for scaling studies and to facilitate testing with alternative propellants that may exhibit poorer ionisation characteristics than argon. Operation with argon was selected as the baseline due to its low cost and availability, but provisions were included to allow reconfiguration for alternative gases. Finally, the thruster was designed with robustness in mind, ensuring it can withstand repeated assembly, disassembly, and handling during training and research activities.

These requirements form the baseline against which subsequent design choices and the overall success of the project will be evaluated.

3.2 Initial Scaling

The design of a Hall thruster involves a large number of coupled parameters, from channel geometry to discharge power and propellant flow. Although high-fidelity plasma simulations can capture these dependencies, they are computationally expensive and impractical for preliminary design. Instead, empirical scaling laws provide a pragmatic starting point. By condensing decades of experimental data into compact relations, they allow first-order estimates of thruster dimensions and operating points to be made rapidly and with reasonable accuracy.

The first stage of the thruster design was to determine a feasible set of discharge channel dimensions and operating parameters consistent with the project requirements. The maximum power available from the laboratory facility was limited to 150 W, while the supply hardware constrained the discharge voltage to a maximum of 300 V. These two values defined the design operating point and served as the inputs for the scaling analysis.

Designing directly from first-principles plasma physics would be intractable at this stage due to the complexity of the governing equations. Instead, empirical scaling relations provide a practical route to dimensioning. In this project, the methodology of Lee et al. [28] was adopted. Their scaling laws were derived from an experimental dataset of predominantly sub-kilowatt Hall thrusters, making them directly applicable to the intended 150 W operating point. For completeness, the full dataset is reproduced in Appendix B.1.

3.2.1 Methodology

The first design parameter to be established was the mean channel diameter. Lee et al. identified a strong correlation between anode power and the product of discharge voltage and squared channel diameter, expressed as

$$P_d = 633 U_d d^2 \quad (3.1)$$

where P_d is the anode power (W), U_d the discharge voltage (V), and d the mean channel diameter (m). This relation reflects the fact that for a given voltage, the discharge volume, and therefore the available ionisation capacity, scales approximately with d^2 .

Substituting the target inputs of $P_d = 150$ W and $U_d = 300$ V yields a mean discharge channel diameter of 28.1 mm. Figure 4 shows that the correlation between anode power and $U_d d^2$ is strong, with relatively little scatter across the dataset. The present design point lies centrally within this cluster, giving confidence that the derived mean channel diameter is robust.

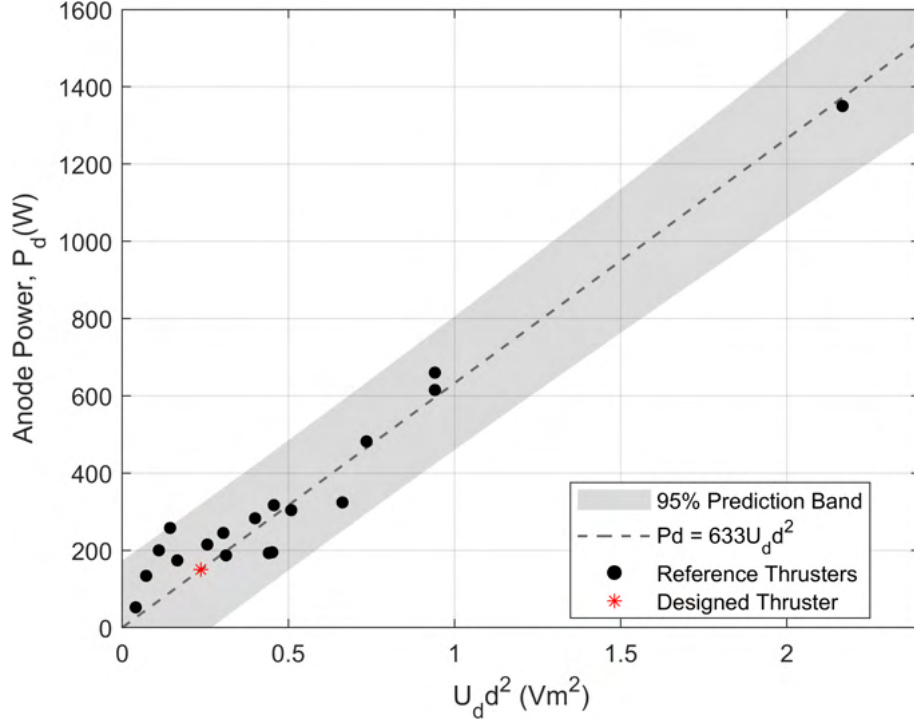


Figure 4: Scaling of anode power with the geometric–electrical parameter $U_d d^2$ for sub-kilowatt Hall thrusters. Black points indicate reference thrusters, the dashed line shows the empirical fit $P_d = 633 U_d d^2$, and the shaded region denotes the 95% prediction band. The present design is marked in red.

With the mean channel diameter determined, the channel width was subsequently estimated. Lee et al. reported a simple proportional relationship between the two parameters:

$$h = 0.242 d \quad (3.2)$$

where h is the channel width (m) and d the mean channel diameter (m). This relation arises from geometric similarity across the reference dataset: as channel size increases, the discharge cross-sectional area must scale proportionally to maintain comparable ionisation and acceleration conditions.

Using the calculated mean channel diameter of 28.1 mm, the resulting channel width is 6.8 mm. Figure 5 demonstrates that the relationship between channel width and mean diameter is somewhat weaker than Figure 4, with greater spread around the fitted line. While the present design follows the expected trend, the increased scatter indicates that predictions of channel width carry greater uncertainty relative to mean channel diameter

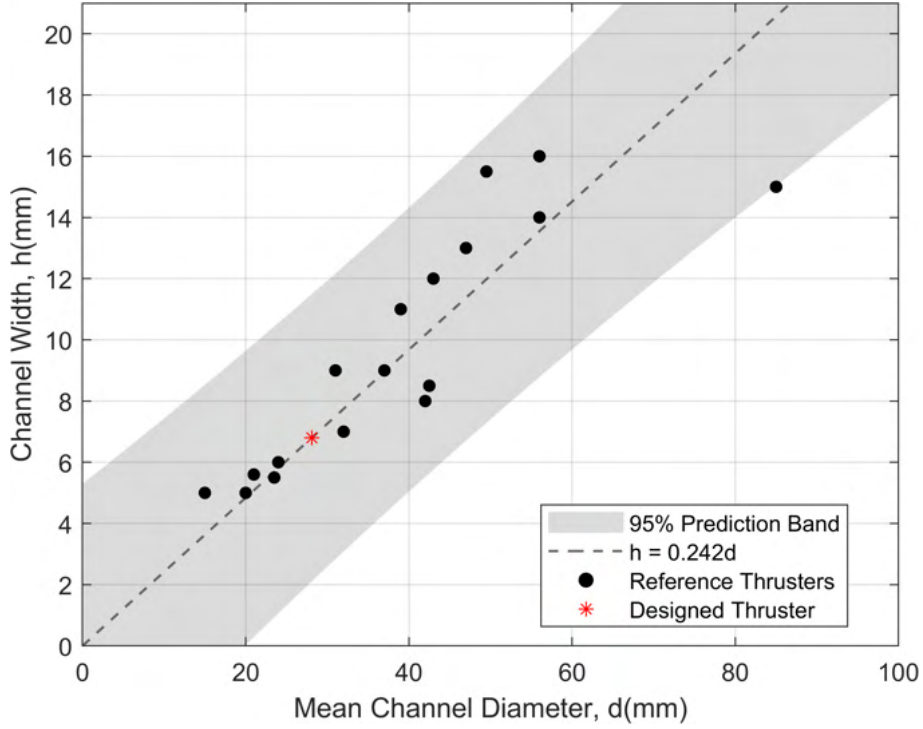


Figure 5: Relationship between mean channel diameter (d) and channel width (h) for Hall thrusters in the reference dataset. The dashed line shows the scaling law $h = 0.242d$, with the shaded region indicating the 95% prediction band. Black points represent reference thrusters, while the red marker denotes the present design.

Once the channel geometry was defined, the corresponding propellant mass flow rate was estimated. Lee et al. established that the anode mass flow rate scales with the product of channel diameter and width according to

$$\dot{m}_a = 0.003 h d \quad (3.3)$$

where \dot{m}_a is the anode mass flow rate (kg/s), h the channel width (m), and d the mean channel diameter (m). Physically, this reflects the requirement that the neu-

tral particle density in the discharge channel remains within the ionisation regime observed across the dataset. A larger channel cross-sectional area requires proportionally greater propellant feed to maintain similar plasma conditions.

Substituting the calculated channel dimensions of $d = 28.1$ mm and $h = 6.8$ mm yields a nominal anode mass flow rate of 0.574 mg/s. As shown in Fig. 6, the scaling of mass flow rate with hd shows greater variability across the dataset, likely caused by differences in propellant utilisation and efficiency between the reference devices.

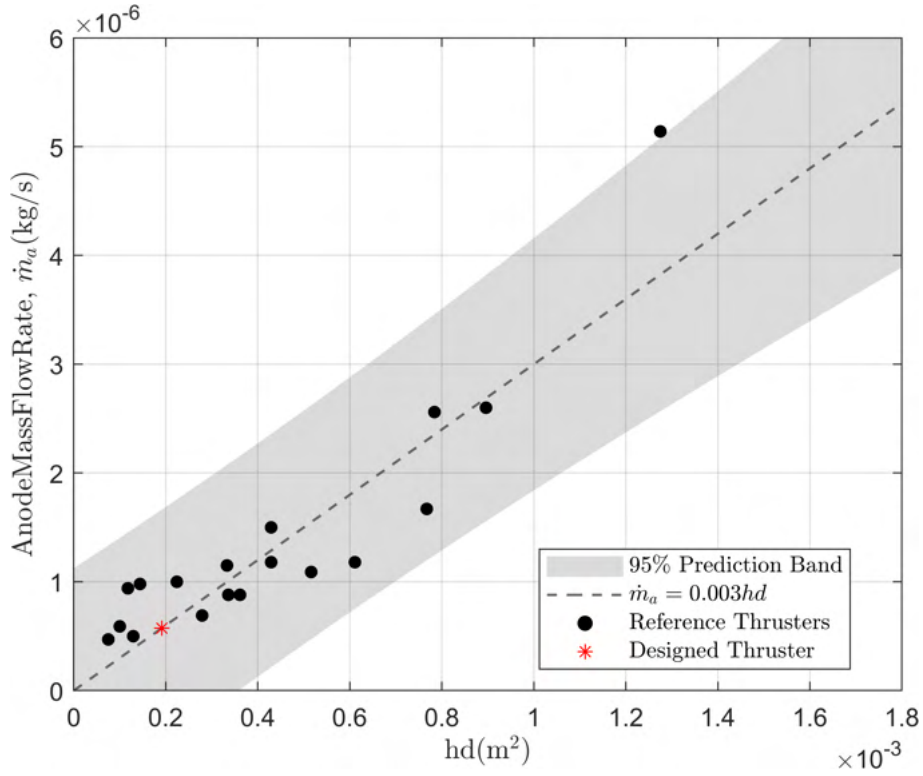


Figure 6: Scaling of anode mass flow rate with the geometric parameter hd for sub-kilowatt Hall thrusters. Black points represent reference devices, the dashed line shows the empirical correlation $\dot{m}_a = 0.003hd$, and the shaded region denotes the 95% prediction band. The present design is indicated in red.

The final step of the scaling procedure was to estimate the thrust output of the device. Lee et al. correlated thrust with the product of anode mass flow rate and the square root of discharge voltage:

$$T = 892.7 \dot{m}_a U_d^{0.5} \quad (3.4)$$

where T is the thrust (N), \dot{m}_a the anode mass flow rate (kg/s), and U_d the discharge voltage (V). This relation reflects the fact that the axial momentum imparted to the ion beam is determined both by the quantity of ions produced (linked to \dot{m}_a) and their exhaust velocity (linked to $U_d^{0.5}$).

Using the calculated mass flow rate of $\dot{m}_a = 0.574$ mg/s and a discharge voltage of $U_d = 300$ V, the predicted thrust is 8.86 mN. The thrust scaling shown in Fig. 7 exhibits a very strong correlation with little scatter about the fitted line. This provides greater confidence in the thrust estimate derived from the scaling law. However, this confidence is contingent on the accuracy of the mass flow rate prediction, which itself is subject to greater variability across the dataset.

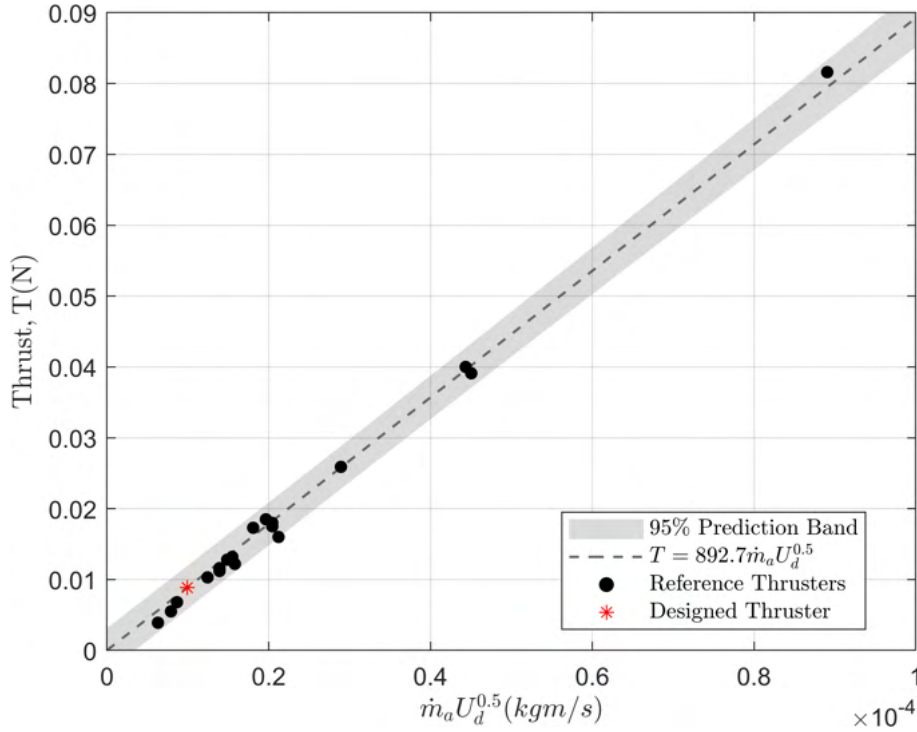


Figure 7: Scaling of thrust with the parameter $\dot{m}_a U_d^{0.5}$ for sub-kilowatt Hall thrusters. Experimental thrusters are shown as black points, the dashed line indicates the empirical correlation $T = 892.7 \dot{m}_a U_d^{0.5}$, and the shaded region represents the 95% prediction interval. The present design point is shown in red.

The scaling relations applied above were derived from a dataset of thrusters operating using xenon. As the present thruster is intended to operate on argon, direct use of xenon-based predictions would be incorrect for performance parameters such as thrust. The principal difference is the ion mass: xenon has $M_{Xe} \approx 131$ amu, whereas argon has $M_{Ar} \approx 40$ amu. For a given discharge voltage, the

single-ion exhaust velocity scales as $v_i \propto M^{-1/2}$ via $v_i \simeq \sqrt{2eU_d/M}$, and the thrust scales as $T \simeq \dot{m}_i v_i$.

In this project the adaptation was made by maintaining the same neutral particle number density in the discharge channel as that implied by the xenon-based scaling point. Practically, this is achieved by reducing the anode mass flow rate in proportion to the atomic mass ratio

$$\dot{m}_{Ar} = \dot{m}_{Xe} \frac{M_{Ar}}{M_{Xe}} \quad (3.5)$$

This preserves the ionisation environment set by the geometry and the chosen position on the xenon-based correlations, whilst acknowledging that the momentum per ion will be smaller for argon.

Under this assumption, the thrust follows a simple scaling factor. With $v_i \propto M^{-1/2}$ and $\dot{m} \propto M$, the thrust scales as

$$T_{Ar} = T_{Xe} \sqrt{\frac{M_{Ar}}{M_{Xe}}} \quad (3.6)$$

Applying these relations to the design point ($\dot{m}_{Xe} = 0.574 \text{ mg/s}$, $U_d = 300 \text{ V}$, $T_{Xe} = 8.86 \text{ mN}$) gives $\dot{m}_{Ar} \approx 0.175 \text{ mg/s}$ and $T_{Ar} \approx 4.90 \text{ mN}$.

It should be noted that the scaling laws do not directly provide a prediction for specific impulse. Instead the adapted outputs for the thruster were used in conjunction with Eq. (1.4) derived in Chapter 1 to determine a theoretical specific impulse.

$$I_{sp} = \frac{T_{Ar}}{\dot{m}_{Ar} g_0}$$

At the design point ($U_d = 300 \text{ V}$, $\dot{m}_{Ar} \approx 0.175 \text{ mg/s}$, $T_{Ar} \approx 4.90 \text{ mN}$), this gives a predicted specific impulse of 2855 s. The real specific impulse will likely be somewhat lower than this but it is a good example of how a lighter propellant gas results in an increased specific impulse at the cost of thrust

The complete set of argon-based parameters taken forward into the magnetic circuit design are summarised in Table 2.

Parameter	Xe Values	Ar Values	Design Values
Mean channel diameter, d (mm)	28.1	28.1	30
Channel width, h (mm)	6.8	6.8	7
Anode mass flow, \dot{m} (mg/s)	0.5735	0.175	0.175
Thrust, T (mN)	8.87	4.90	4.90
Specific impulse, I_{sp} (s)	1577	2855	2855

Table 2: Summary of design parameters derived from Lee et al.’s xenon scaling laws, adapted for argon, and final values selected for the design.

3.3 Magnetic Circuit Design

With the channel geometry, mass flow rate, and target operating point established, attention now turns to the magnetic circuit. The scaling process provided the physical envelope of the discharge channel, but for the thruster to function the magnetic field must be tailored to this geometry. Specifically, the circuit must generate a radial field strong enough to magnetise electrons ($r_e \ll L$), while leaving ions unmagnetised ($r_i \gg L$) thereby sustaining the Hall current and maintaining the potential drop required for acceleration. The design of the magnetic circuit therefore forms the next step in translating the scaling-derived parameters into a practical thruster configuration.

The design process followed a structured sequence: (i) defining candidate coil layouts consistent with the geometry, (ii) selecting a baseline arrangement, (iii) simulating the magnetic topology using Finite Element Analysis (FEA) in Ansys Maxwell, (iv) iterating coil parameters such as the number of turns, wire gauge, and core dimensions, and (v) evaluating the resulting field profile against confinement and plasma depth requirements.

3.3.1 Coil Layout Subsection

Several coil configurations are used in Hall thruster design, each suited to different scales and operating regimes. The choice of layout for this project was guided by the discharge channel geometry derived from the scaling laws, the 150 W design point, and the need to balance plasma physics requirements with manufacturability.

Outer-only coils: Some very low-power thrusters dispense with a central winding and rely solely on outer coils to shape the field. This simplifies construction, but

without an inner coil the field strength near the channel axis is relatively weak and less controllable, leading to poorer confinement uniformity. These layouts remain viable only in the lowest power ranges (tens of watts or below), where the small discharge channel naturally demands high magnetic field strengths, and the geometry is compact enough that outer coils alone can impose the required field shape. As thrusters scale up in size and power, the magnetic field strength requirement decreases, but maintaining the correct radial topology across a wider channel becomes more difficult. In these cases, outer-only coils cannot provide sufficient field uniformity, and a central coil becomes necessary.

Dual or segmented inner coils: At the opposite extreme, some high-power thrusters employ dual or segmented inner windings to fine-tune the axial field gradient and improve lifetime. These approaches add complexity and are impractical at the sub-kilowatt scale due to limited space for windings and structural components. They are also often combined with centrally mounted hollow cathodes, which cannot be accommodated in the compact geometry of the present design and are generally reserved for larger devices.

Single central plus outer coils (baseline): For mid-power thrusters such as the present 150 W design, a configuration with a single central coil and multiple outer coils provides the most effective balance. The central coil strengthens the field near the axis, reducing radial variation in confinement, while the outer coils complete the return path and establish the radial field at the channel exit. The number of outer coils has a direct impact on the uniformity and controllability of the magnetic field. With fewer coils, the circuit is simpler to manufacture and operates with lower resistance, but the resulting field tends to be less uniform across the discharge channel. Adding more coils improves field shaping and uniformity, particularly in larger thrusters where greater coil spacing can otherwise lead to uneven confinement. However, this comes at the cost of increased winding resistance, packaging complexity, and manufacturing time.

For this design, four outer coils were selected as an appropriate balance, based on several comparable thrusters and their coil configurations [29, 30, 31]. At the 150 W scale the geometry is small enough that field uniformity is not critically compromised by limiting the coil count, yet four coils provide sufficient control of the discharge region without making the design impractical to build.

3.3.2 2D Model

To evaluate the magnetic circuit, a parametric 2D model of the thruster was constructed within Ansys Electronics Desktop (AEDT). Due to the azimuthal symmetry of the chosen layout the problem could be reduced to a planar slice intersecting the central coil and two opposing outer coils. This simplification allowed the magnetic field distribution to be studied efficiently whilst retaining the essential topology of the circuit.

Table 3 lists the fixed geometric parameters applied to the model, derived directly from the initial scaling analysis and some manufacturing specific limits. Figure 8 shows the resulting 2D cross-section of the model geometry.

Parameter	Value	Unit
Mean Channel Diameter	30	mm
Channel Width	7	mm
Coil Core Width	6	mm
Coil Wire Diameter	0.51 24	mm AWG
Magnetic Core Base Thickness	5	mm
Magnetic Core Pole Thickness	3	mm
Magnetic Pole Overhang	2	mm
Boron Nitride Wall Thickness	5	mm
Boron Nitride Base Thickness	6	mm

Table 3: 2D Model Fixed Input Parameters

The plasma-facing dimensions (mean channel diameter and channel width) were taken directly from the scaling process. The boron nitride thicknesses were selected to provide adequate lifetime against erosion and to ensure sufficient mechanical robustness, given the brittle and relatively soft nature of the material. The magnetic core dimensions (base and pole thicknesses) were constrained by the availability of stock material, while the pole overhang was set to mechanically retain the boron nitride inserts without excessively reducing the effective insert thickness. The coil wire diameter was limited to 0.51 mm (24 AWG) to remain compatible with the available winding tool, setting the practical upper bound on conductor size.

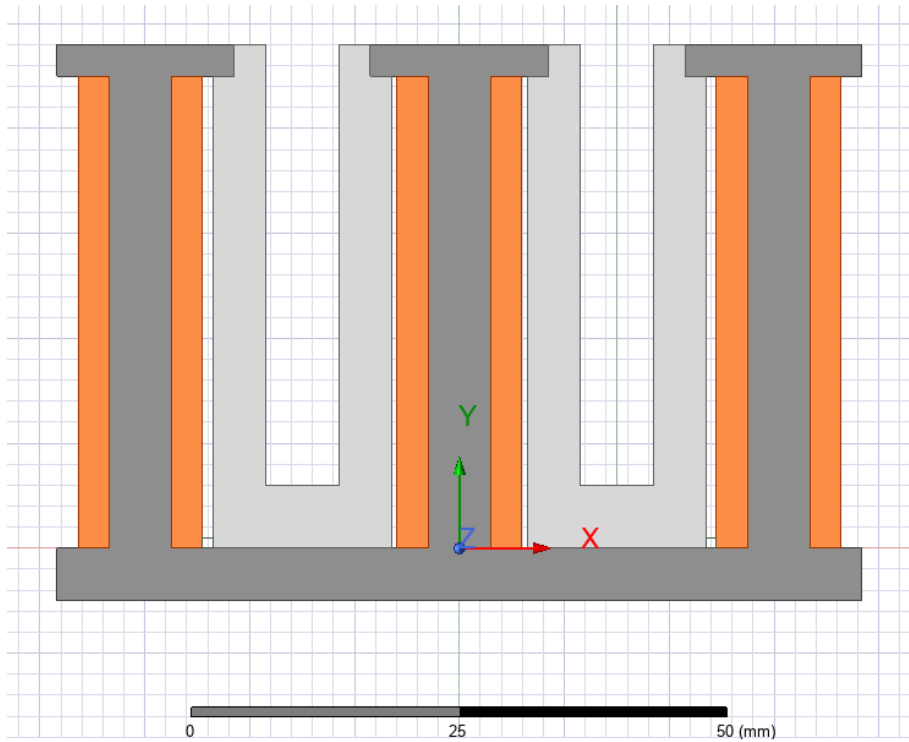


Figure 8: 2D parametric model of the thruster magnetic circuit in Ansys Maxwell, showing magnetic cores (grey), coils (orange), and discharge channel (white).

The Material properties were assigned from the AEDT library. The magnetic circuit was modelled in 1008 steel (dark grey) to provide a high-permeability flux return path, whilst the windings were modelled as copper (orange). The discharge channel insert, composed of boron nitride, was assigned vacuum properties as its magnetic permeability is negligible; however, the geometry was retained in the model to ensure correct coil spacing.

3.3.3 Simulation Setup

The analysis of the magnetic circuit was carried out using the magnetostatic solver within AEDT, which calculates the steady-state magnetic field produced by current-carrying conductors. Time-dependent effects such as eddy currents and plasma–magnetic coupling were neglected at this stage, as the objective was to determine the coil configuration required to generate the desired static field topology.

The simulation domain was extended to a radius several times greater than the thruster body, and open boundary conditions were applied at the outer edges. This prevented artificial confinement of the flux and allowed field lines to expand

naturally into the free space at the channel exit.

Coils were represented as current-driven windings with user-defined turn counts, conductor cross-sections, and operating currents. A parametric sweep was then performed over the following key variables

- The Number Of Turns Per Coil
- The Operating Coil Current
- The Discharge Channel Length

The optimisation criteria were drawn directly from the confinement conditions introduced in Chapter 2. The radial magnetic field within the discharge channel needed to be strong enough that the electron Larmor radius remained much smaller than the plasma depth, thereby ensuring effective confinement. At the same time, the field had to remain weak enough that the ions were unaffected. In practice, this translated into achieving a minimum field strength of approximately 15 mT across the intended plasma depth, while limiting the peak field at the channel exit to below 350 mT.

3.3.4 Short Configuration Results

The short channel configuration was first evaluated to establish a baseline magnetic topology. The coil design was constrained by both geometry and thermal considerations. For the central coil, the winding count was limited by the need to remain fully contained within the boron nitride insert. In practice, this restricted the coil to a maximum of 600 turns before intersecting the channel insert. To maintain a balanced and predominantly radial field at the channel exit, the outer coils were also limited to 600 turns.

With winding count fixed, the primary control variable became the coil current. This was constrained by the current-carrying capacity of the selected 24 AWG enamelled copper wire. The maximum allowable coil current is constrained by thermal limits, since in a vacuum, cooling is provided almost exclusively by radiation and limited conduction to the magnetic core. A simple heat balance can be used to estimate the maximum current in a winding. Equating resistive heating to net radiative loss gives

$$I^2 R = f_v \epsilon \sigma A_s (T_w^4 - T_s^4) \quad (3.7)$$

where I is the current, $R = \rho L / A_c$ the wire resistance, ρ is the copper resistivity, L is the wire length, $A_c = \pi d^2 / 4$ the conductor cross section, $A_s = \pi d L$ the surface area, ϵ the effective emissivity of the enamelled copper surface, σ the Stefan-Boltzmann constant, T_w the wire temperature, T_s the ambient temperature, and f_v an effective view factor accounting for self-viewing between adjacent turns. The length cancels, giving the closed form expression independent of coil size

$$I_{max} = \sqrt{\frac{\epsilon f_v \sigma (\frac{\pi^2}{4}) d^3 (T_w^4 - T_s^4)}{\rho}} \quad (3.8)$$

For the 24 AWG enamelled copper wire used in this design ($d = 0.511 \text{ mm}$, $\rho \approx 2 \times 10^{-8} \Omega \text{ m}$, $\epsilon \approx 0.8$), with a background temperature of 300 K, the maximum sustainable current depends on the wire temperature limit and view factor. For a conservative effective view factor of $f_v = 0.015$, corresponding to tightly packed coil where most radiation is reabsorbed, the current limits are found to be approximately 0.6 A for short-term operation (wire at 150°C) and 0.4 A for continuous operation (wire at 120°C). This estimate is conservative, as it neglects conductive heat transfer into the magnetic core and adjacent coil turns. In practice, these conduction paths would increase the allowable current somewhat, but 0.5 A remains a sensible upper bound for short-duration operation. To provide experimental validation of these limits, a thermocouple may be affixed to one of the coils, enabling direct monitoring of coil temperature during operation.

The final parameters adopted for the short configuration are summarised in Table 4.

Parameter	Value	Unit
Mean Channel Diameter	30	mm
Channel Width	7	mm
Channel Length	42	mm
Inner Core Windings	600	turns
Outer Core Windings	600	turns
Wire Diameter	0.51 24	mm AWG
Coil Current (Short Duration)	0.5	A
Coil Current (Continuous)	0.35	A
Coil Length	45	mm

Table 4: Summary of short configuration parameters used in magnetic circuit modelling.

Figure 9 shows the vector potential distribution and associated flux lines generated by this coil set. A clear magnetic lens forms at the channel exit plane, a characteristic feature of unshielded SPTs. The return path is well defined through the high-permeability steel, with flux emerging radially across the channel exit before closing through the outer return legs. The central coil effectively strengthens the field near the axis, reducing asymmetry across the channel span.

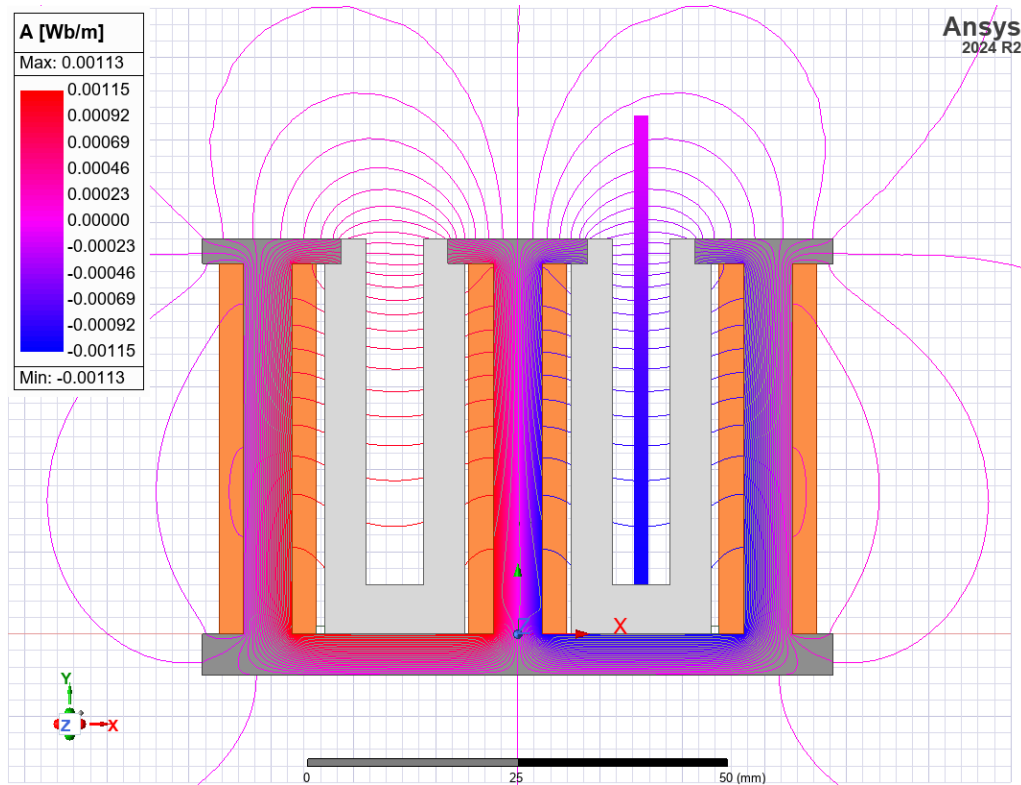


Figure 9: Magnetic vector potential distribution and flux lines for the short configuration.

The corresponding magnetic flux density is shown in Figure 10. The field is concentrated near the channel exit plane, peaking at approximately 110 mT at the pole tips, before expanding outward into free space. This localisation of the peak field is advantageous, as it promotes ionisation and acceleration in the exit region while limiting excessive confinement deeper in the channel.

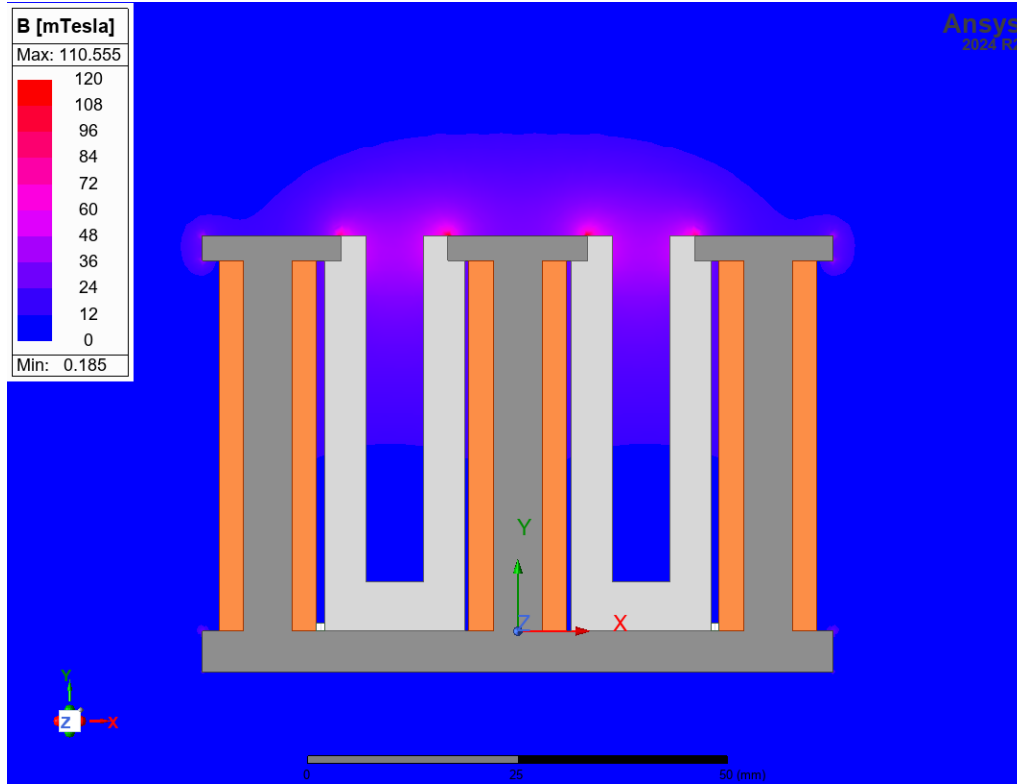


Figure 10: Magnetic flux density distribution for the short configuration.

To quantify the field variation, the axial magnetic field strength was sampled along the channel centreline for a range of coil currents (Figure 11). At 0.5 A per coil, the field exceeds 15 mT for approximately 20 mm inside the channel, suggesting that the plasma can be sustained across this depth. Beyond the exit plane the field falls sharply, consistent with behaviour reported for similar SPTs and desirable for allowing ions to accelerate freely downstream.

When these results are interpreted alongside the coil current limits derived above, an important trade-off becomes clear. For short-duration operation at 0.5 A, the plasma depth extends to around 20 mm, making near-optimal use of the available channel length. For continuous operation, however, the current must be reduced to about 0.35–0.4 A to remain within thermal limits. At these lower currents the centreline profile indicates that the 15 mT threshold is only maintained over roughly 12–15 mm, reducing the effective plasma depth and therefore ionisation efficiency.

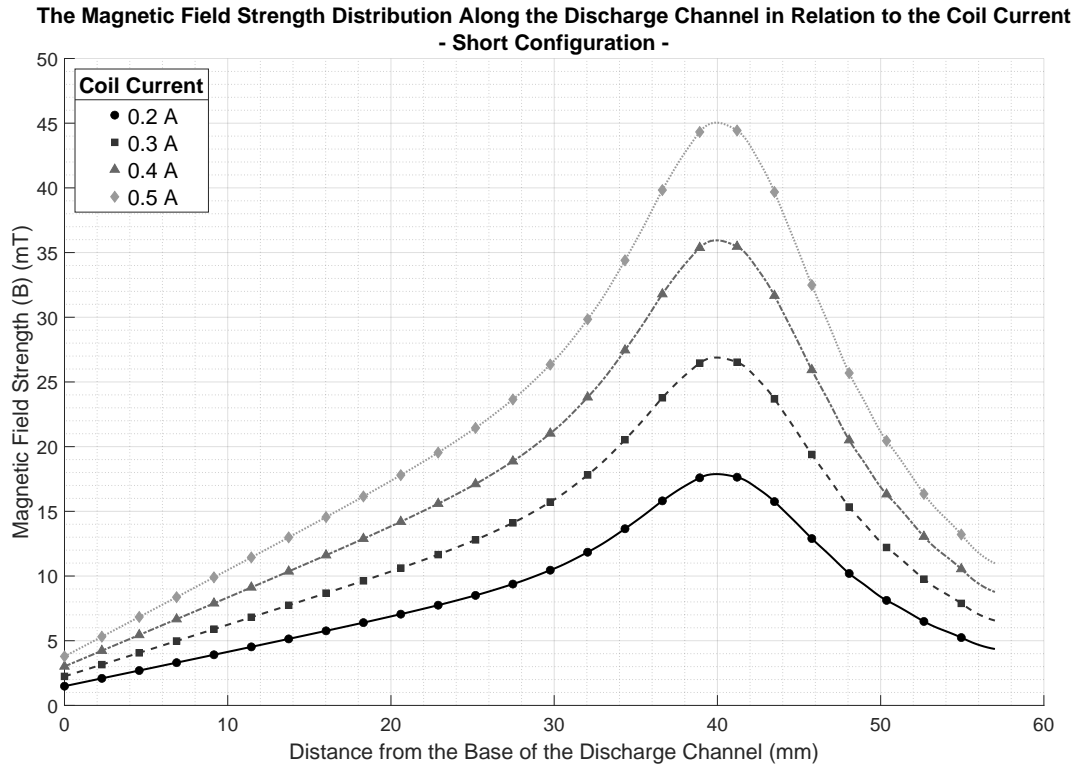


Figure 11: Axial magnetic field strength along the channel centreline for the short configuration at different coil currents.

In summary, the short configuration shows that the selected coil layout produces the expected magnetic lens at the channel exit and can sustain a plasma depth of up to 20 mm during short-duration operation. However, the effective confinement length is strongly constrained by coil thermal limits, reducing to only 12–15 mm under continuous operation. This sensitivity to thruster operation time provides the motivation for evaluating the long-channel configuration, where a deeper ionisation region and longer coils may compensate for reduced coil current.

3.3.5 Long Configuration Results

To evaluate the impact of extending the discharge channel, a long configuration was modelled using the same coil windings and current limits defined for the short case. The principal change was the channel length, which was increased to 65 mm. This adjustment allowed the confinement region to extend further downstream, potentially increasing the ionisation depth available under continuous operation. The adopted parameters are summarised in Table 5.

Parameter	Value	Unit
Mean Channel Diameter	30	mm
Channel Width	7	mm
Channel Length	65	mm
Inner Core Windings	900	turns
Outer Core Windings	900	turns
Wire Diameter	0.51 24	mm AWG
Coil Current (Short Duration)	0.5	A
Coil Current (Continuous)	0.35	A
Coil Length	68	mm

Table 5: Summary of long configuration parameters used in magnetic circuit modelling.

Figure 12 shows the magnetic vector potential distribution for the long configuration. As in the short case, a magnetic lens forms at the channel exit, but the extended winding length and increased turn count cause the field to penetrate more deeply into the discharge channel. The flux remains well confined by the steel core, with symmetry across the channel axis preserved.

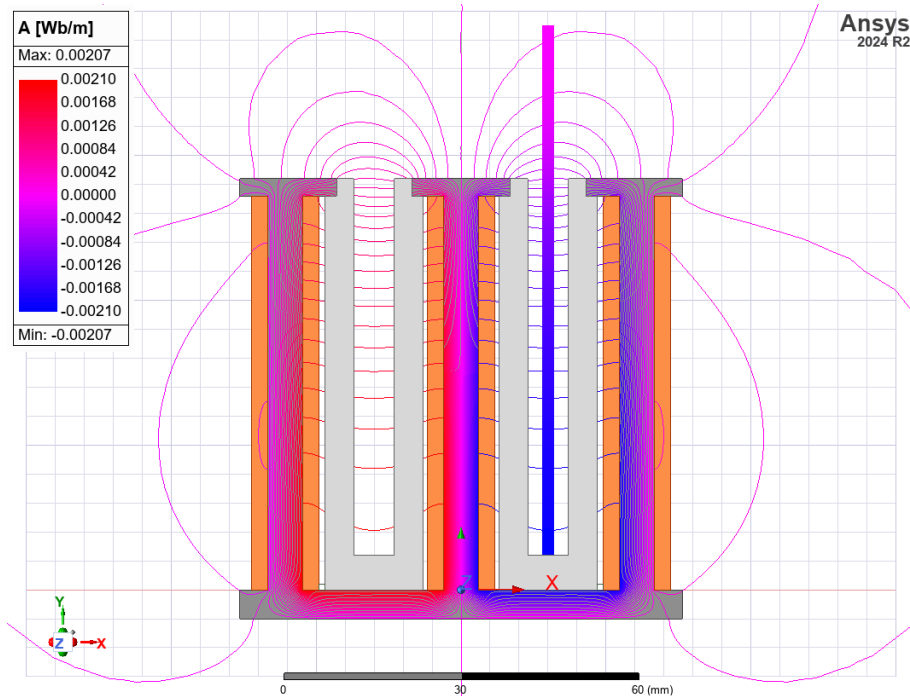


Figure 12: Magnetic vector potential distribution and flux lines for the long configuration.

The corresponding magnetic flux density is shown in Figure 13. Compared with the short configuration, the peak field at the channel exit is slightly higher at 181 mT, the higher winding count also sustains the field strength further upstream. This results in a more gradual decay along the channel, broadening the ionisation region while still preserving a strong lens at the exit.

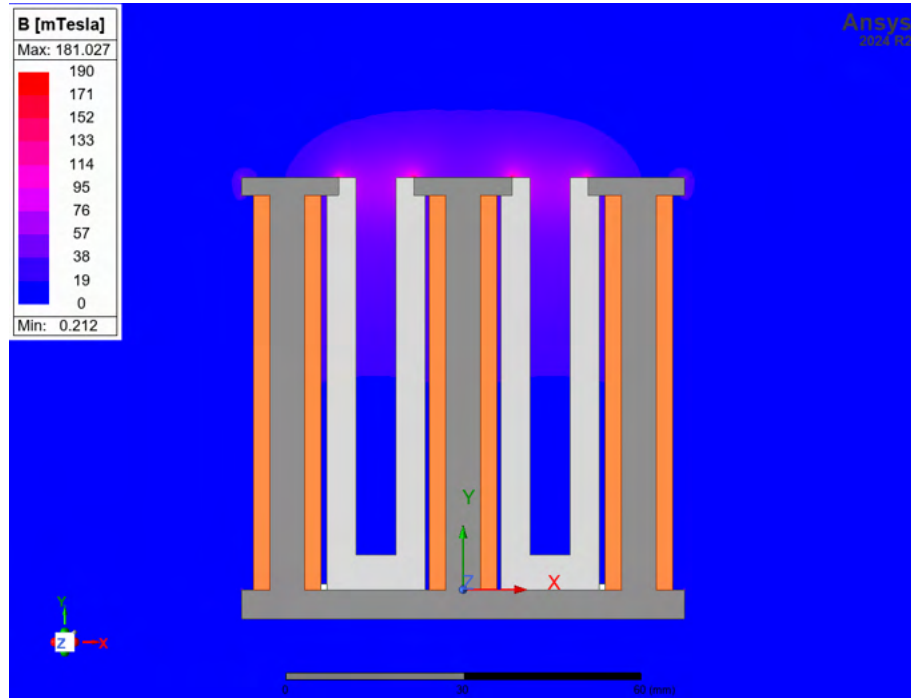


Figure 13: Magnetic flux density distribution for the long configuration.

The axial centreline field profiles are plotted in Figure 14. At 0.5 A per coil, the 15 mT threshold is sustained for nearly 47 mm of channel depth, over twice the confinement length of the short configuration. Under continuous operation at 0.35–0.4 A, the effective plasma depth remains in the range of 39 - 35 mm, representing a significant improvement compared with the 12–15 mm sustained by the short channel. The falloff beyond the channel exit is sharper with the long configuration.

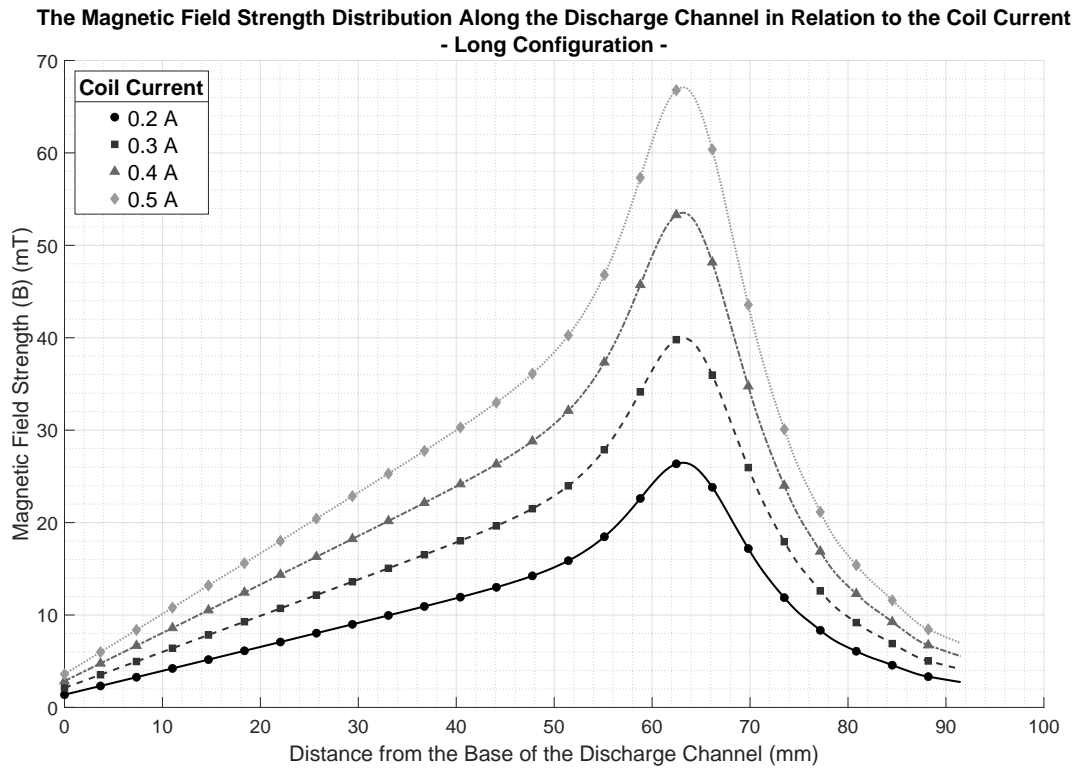


Figure 14: Axial magnetic field strength along the discharge channel centreline for the long configuration at different coil currents.

In summary, the long configuration provides a clear advantage in sustaining plasma depth under both short-duration and continuous operation. The additional coil windings extend the ionisation region significantly, making performance less sensitive to the thermal limits of the coils. However, the increased penetration of the magnetic field also raises the likelihood of ion–wall interactions deeper within the channel, which may accelerate erosion of the boron nitride inserts. In practice, the adjustable anode position provides a degree of control over the active plasma depth, allowing the ionisation region to be shifted within the channel to balance performance against lifetime. The trade-off therefore lies not only in increased coil resistance and manufacturing complexity, but also in managing erosion risk, though at this scale the benefits to plasma confinement remain substantial.

3.4 Detailed Design

With the scaling analysis and magnetic circuit simulations completed, the next stage of the project was to translate the selected configuration into a manufac-

turable thruster. This required building a full 3D model in SolidWorks, specifying materials, and planning the ancillary systems needed for laboratory testing. Unlike the preceding stages, which were primarily analytical, this phase was driven by practical considerations: material availability, manufacturing constraints, and lead times.

3.4.1 Mechanical Design and CAD Modelling

The overall thruster design draws heavily upon the work of Lee [29], whose master's thesis presented a manufacturable sub-kilowatt SPT configuration. That design provided a practical foundation for this project, particularly in terms of component layout. The present configuration was adapted to incorporate two interchangeable channel lengths, operate with argon rather than xenon propellant, substitute materials compatible with the UK supply chain, and suit the manufacturing capabilities of the available workshop.

The discharge channel was the first major component to be finalised. Because it required machining from boron nitride, a brittle material with limited suppliers and long lead times, its design had to be frozen early and sent for manufacture well ahead of other parts. The CAD model was used to carefully define wall thicknesses and tolerances, balancing the need for robustness against erosion with the fragility of the material. The design of the discharge channel and magnetic circuit components was undertaken in parallel with AEDT simulations, ensuring that the geometries tested numerically were representative of what could actually be manufactured, while also allowing long-lead components such as the boron nitride inserts to be ordered without delaying optimisation work.

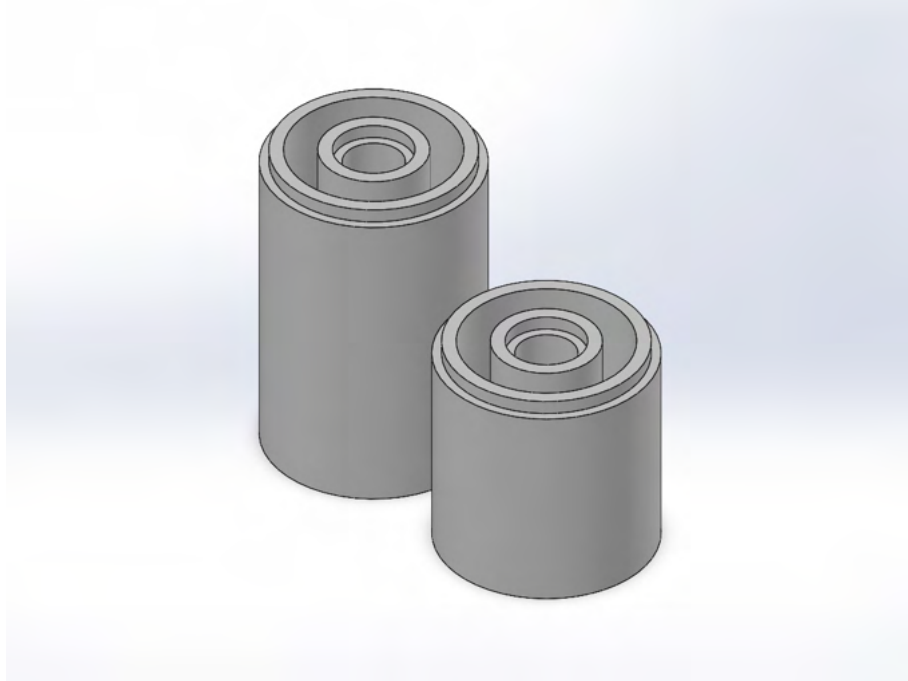


Figure 15: Isometric CAD view of the boron nitride discharge channel insert.

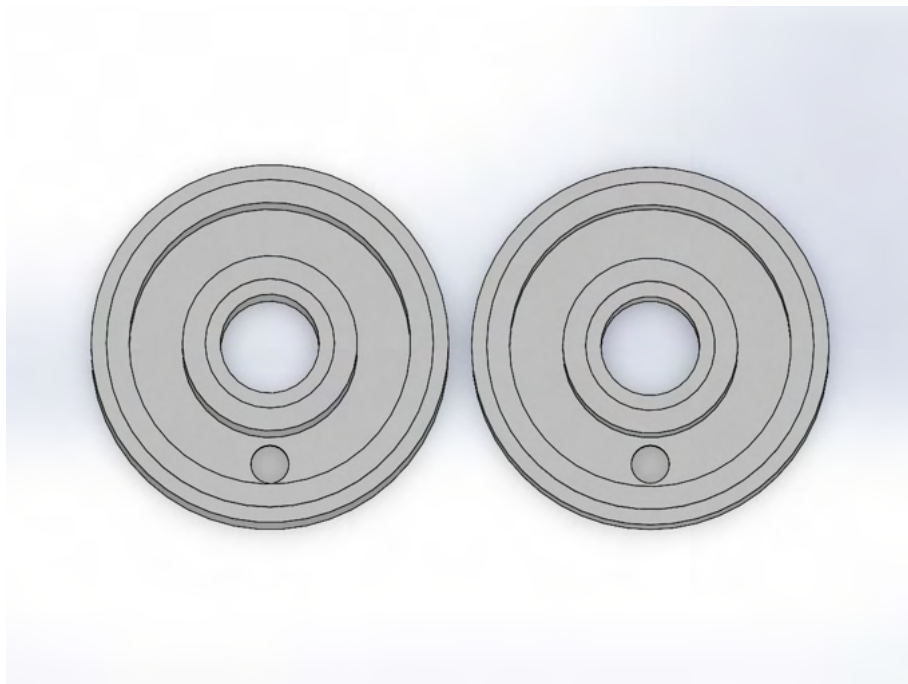


Figure 16: Top-down CAD view of the boron nitride discharge channel insert.

The coil regions were modelled in CAD as simplified volumes rather than explicit windings. This avoided unnecessary complexity while still preserving the correct allowances for winding count, wire diameter, and insulation thickness. These coil

regions were dimensioned directly from the requirements identified in the magnetic circuit simulations, ensuring sufficient space for the specified turn count without intersecting the channel inserts. The associated steel magnetic cores and pole pieces were also modelled simultaneously, with their geometry refined to balance magnetic field strength against manufacturability and robustness.

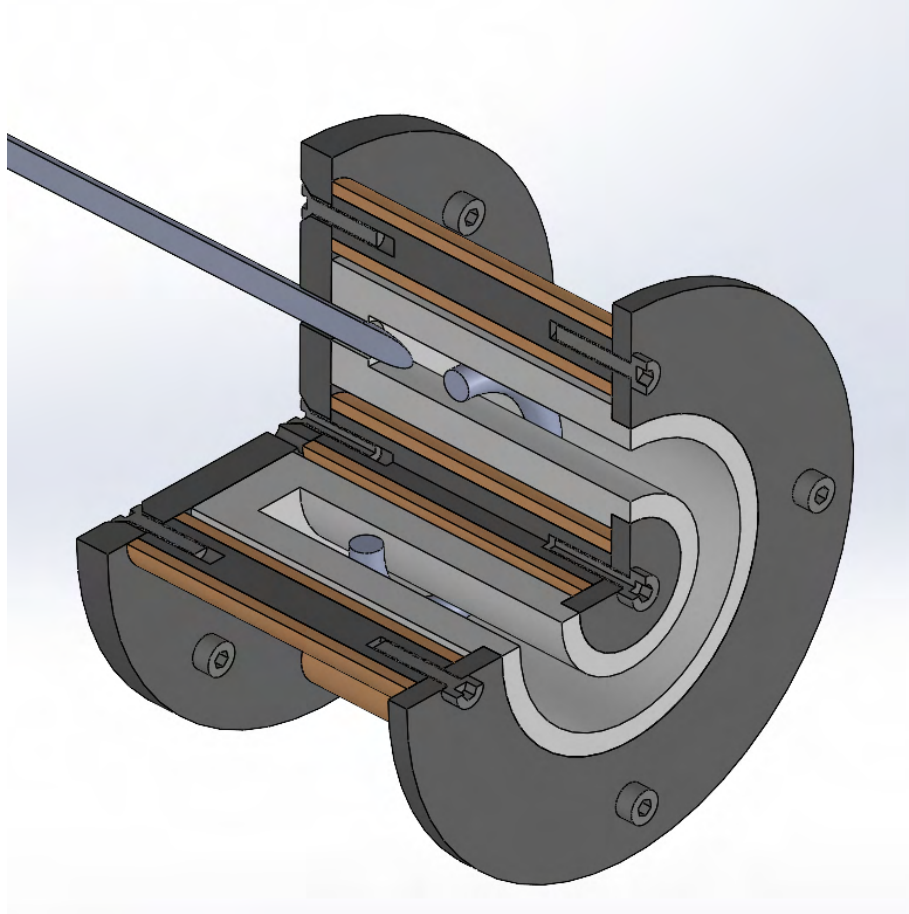


Figure 17: CAD model of the short configuration, showing discharge channel, coil regions, and supporting magnetic cores.

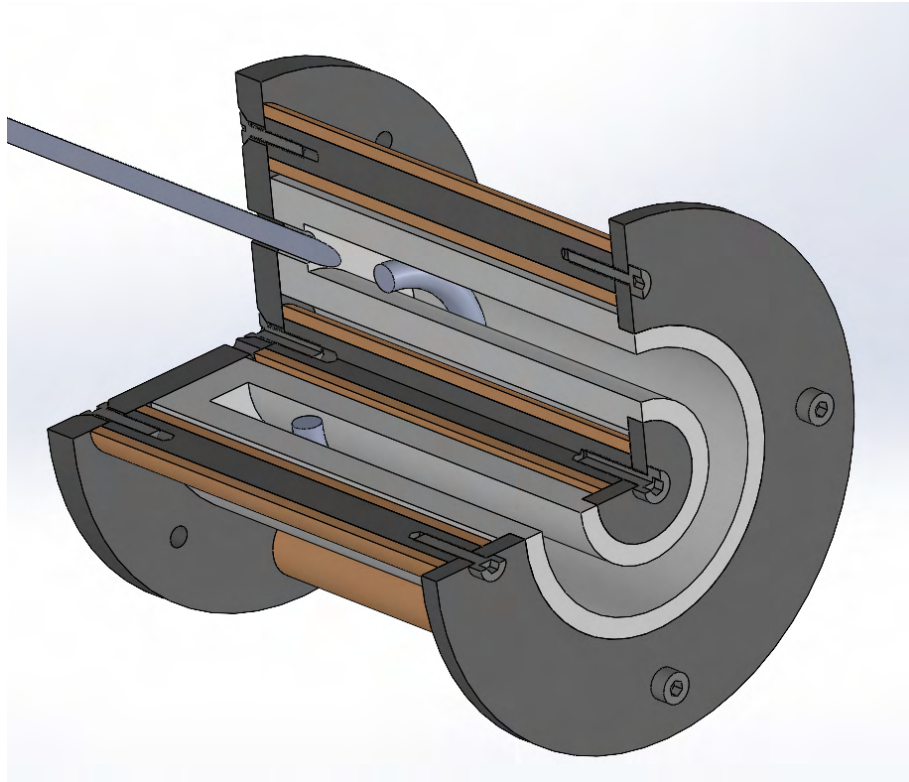


Figure 18: CAD model of the long configuration, showing extended discharge channel and increased coil winding allowance.

The magnetic base and pole pieces were designed with manufacturability as a primary constraint. Both components were dimensioned so that they could be machined directly from standard round stock, requiring only straightforward operations such as drilling, facing, and countersinking. Of these parts, only the baseplate and outer pole were outsourced to external suppliers, alongside the boron nitride channel inserts, as they required equipment not available in-house. In contrast, the inner pole and coil cores were designed around stock diameters available from commercial suppliers, allowing them to be manufactured internally with minimal machining. The mounting holes in both the base and pole pieces were deliberately oversized to provide clearance, ensuring that the coils could be hand-fitted during assembly without risk of binding.

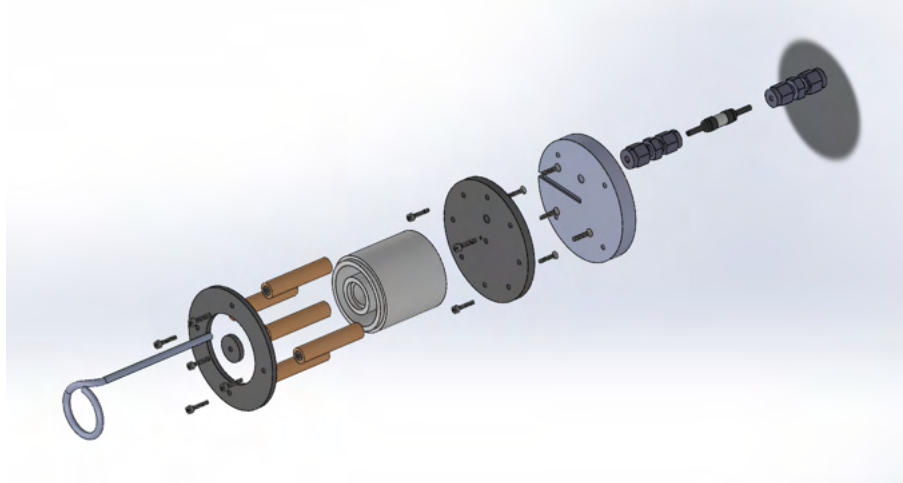


Figure 19: Exploded CAD view of the thruster assembly, showing channel insert, coils, magnetic circuit, and supporting structure.

At the system level, the exploded CAD view illustrates how the thruster will be assembled and disassembled. This was a key design consideration, since the coils, channel inserts, and pole pieces must be removed repeatedly for testing, reconfiguration, and inspection. The mounting plate at the base was designed to be 3D printed in PET-CF with minimal infill, a material selected for its superior thermal and mechanical properties compared to standard PLA. Because the final vacuum-chamber mounting solution has not yet been specified, the use of a 3D-printed plate provides a flexible and low-cost means of prototyping, whilst still allowing the thruster to be mounted securely until a permanent fixture is manufactured.

To validate the robustness of the CAD model before committing to manufacture, several components were produced using 3D printing. These mock-ups allowed the fit of the components to be physically checked, ensuring that tolerances and assembly clearances were realistic. The printed models also provided an early indication of structural robustness and gave confidence that the overall thruster could be assembled with the intended tooling. They were particularly useful for refining the assembly and fastening strategy, ensuring that the fragile boron nitride inserts could be installed and removed without risk of fracture.

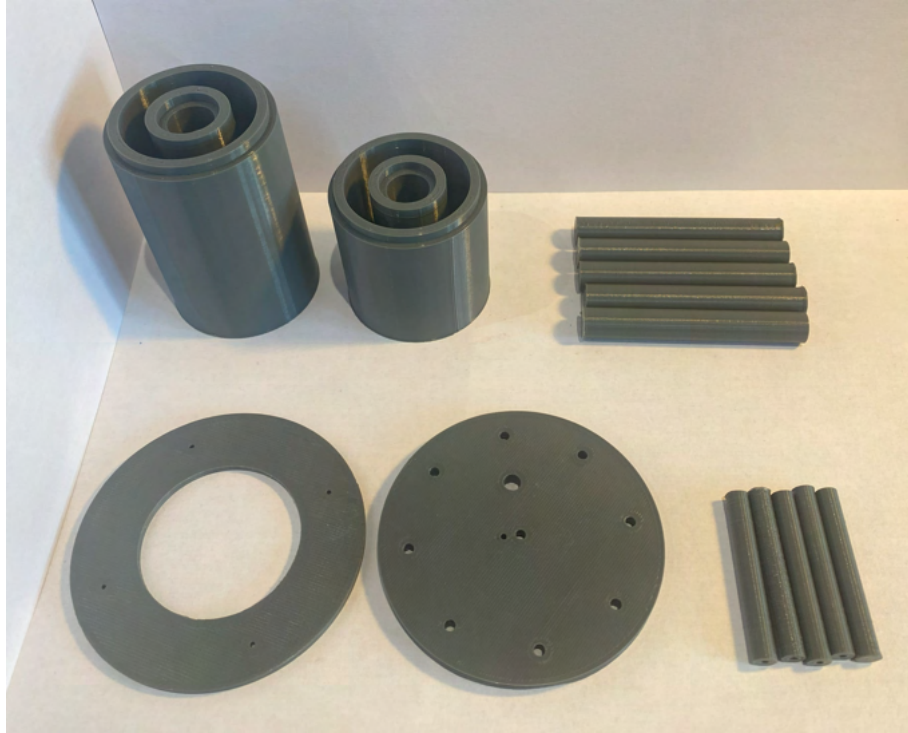


Figure 20: 3D printed mock-ups used to validate assembly, fit, and robustness of the CAD model.

3.4.2 Magnetic Material Substitution

A critical element of the thruster design was the choice of steel for the magnetic circuit components. The requirements for this application are broadly consistent with any 'soft magnetic' material. High magnetic permeability to concentrate the field within the discharge channel, low coercivity to minimise hysteresis losses, and a sufficiently high saturation flux density to prevent local field collapse at the pole tips. At the same time, the material must be available in machinable stock forms suitable for bases, poles, and coil cores.

Previous thruster designs, including Lee [29], have commonly used AISI 1008 steel for this purpose. Its very low carbon content (< 0.1 wt%) gives it excellent magnetic properties while remaining relatively easy to machine. However, 1008 is not a standard grade in the UK and is difficult to source in small quantities, making it impractical for this project.

Instead, EN1A (also known as 230M07) was selected as a substitute. EN1A is a low carbon free cutting steel widely available in both bar and plate stock, and can therefore be easily machined into all required coil cores, pole pieces, and

baseplates. Its carbon content (< 0.15 wt%), is low enough to provide reasonable magnetic performance, while its low cost and ease of machining make it well suited for a laboratory-scale prototype. Alternative options such as electrical steels were considered, but these are generally supplied only as thin laminations for transformer cores and are not available in the solid geometries required for this design.

Although EN1A is unlikely to exactly match the magnetic performance of 1008, its combination of availability, machinability, and cost made it the most practical choice. The real thruster's magnetic circuit may therefore perform slightly below the values predicted in simulation, but any reduction is expected to be marginal and should not significantly affect the achievable plasma depth.

3.4.3 Propellant Feed System

The propellant feed system was designed to deliver a controlled flow of argon into the discharge channel while ensuring compatibility with the vacuum facility and electrical isolation of the thruster. Figure 21 illustrates the overall setup. Argon is supplied from a standard high-pressure bottle, as commonly used in industrial and welding applications, making it inexpensive and readily available. The bottle has a standard regulator which feeds into an Alicat mass flow controller for finer control. This represents the most expensive element of the system but is critical to achieving reliable operation.

The design mass flow rate of $\dot{m}_{Ar} = 0.175$ mg/s was converted into standard cubic centimetres per minute (SCCM) using a simple script (Appendix B.2), yielding a requirement of approximately 5.9 SCCM at standard conditions. Based on this, a 10 SCCM Alicat MFC was selected. This range provides sufficient resolution to control low flow rates with high precision while leaving some overhead capacity for experimental flexibility. The controller is suitable for a wide variety of gases, including mixtures, and can be integrated with a data acquisition computer, allowing both real-time monitoring and control of flow rate.

From the controller, the gas is routed through a bulkhead fitting into the vacuum chamber. Inside the chamber, a short flexible line connects to a high-voltage ceramic break manufactured by Lesker, rated to 5 kV and specifically designed to operate within a vacuum. This ensures electrical isolation between the stainless steel anode, the vacuum chamber walls, the propellant feed lines. Both sides of the ceramic break are fitted with Swagelok connectors, chosen for their reliability

and ease of assembly.

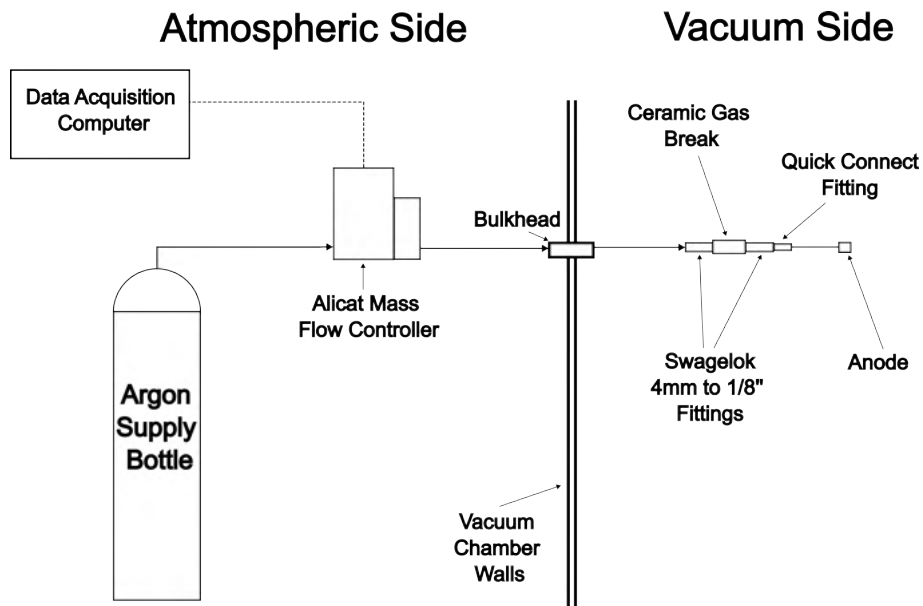


Figure 21: Schematic of the propellant feed system, showing argon supply, mass flow control, vacuum chamber interface, electrical isolation, and anode connection.

The anode was modelled in CAD and is shown in Figure 22. It is fabricated from a single section of 304 stainless steel tubing (4 mm outer diameter, 2 mm inner diameter), bent to follow the channel profile. The use of seamless tubing simplifies manufacture and minimises the risk of leaks. To distribute propellant into the discharge channel, seven 1.5 mm holes were drilled into the rear face of the anode. This geometry was selected as a pragmatic compromise, it is simple to manufacture and expected to provide adequate distribution at the low flow rates of a laboratory-scale prototype. Ideally, the design would be validated through fluid simulations to confirm flow uniformity; however, this could not be completed within the time frame of the present work. Some asymmetry in local density therefore cannot be ruled out, and future work could investigate alternative arrangements such as finer multi-hole arrays or slotted feeds to improve uniformity and reduce erosion risk.

The anode design also prioritises ease of replacement. It slides into position through the front of the thruster and connects directly to ceramic break via a quick connect, allowing it to be exchanged without disassembling the rest of the thruster. This feature makes it straightforward to trial alternative geometries or replace worn components during testing, an important consideration for a laboratory prototype.

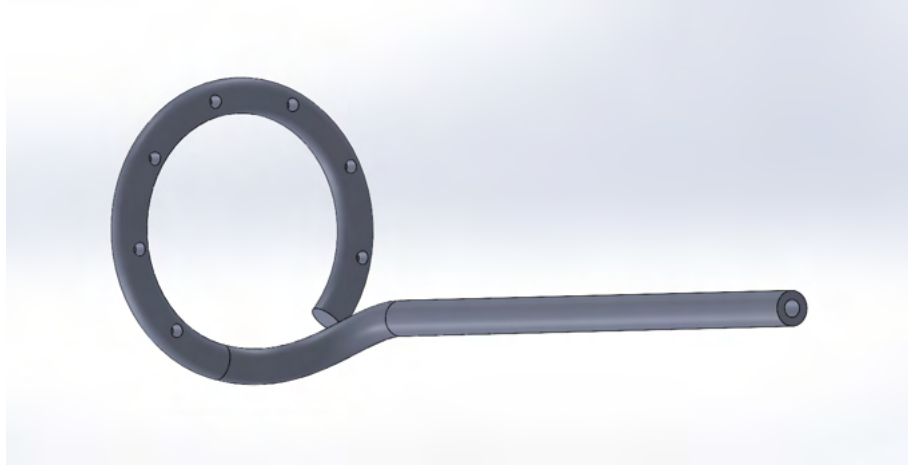


Figure 22: CAD model of the anode and propellant feed interface.

3.4.4 Cathode Integration

A cathode is an essential element of any Hall effect thruster, serving two critical functions: it provides the source of electrons required to ionise the incoming neutral propellant, and it neutralises the ion beam at the thruster exit. Without neutralisation, the accelerating ions would charge the spacecraft negatively, quickly halting thrust production.

Cathode integration in Hall thrusters is typically realised in one of two ways. Larger thrusters often employ a centrally mounted hollow cathode, placed along the axis of symmetry. This arrangement provides efficient electron injection into the discharge channel but requires significant space at the channel centreline, making it impractical for compact geometries. Smaller thrusters instead use externally mounted cathodes, located adjacent to the discharge channel exit. Although external cathodes can lead to less uniform electron distribution, they offer greater flexibility in positioning and are far easier to implement in restricted geometries.

In this project, the cathode will be externally mounted. The decision was driven primarily by geometry. The relatively small channel diameter precludes a central cathode without compromising coil placement. An external configuration also offers experimental flexibility, as the cathode position can be adjusted during testing to optimise coupling with the plasma.

A second design choice was the use of a thermionic cathode based on tungsten filaments rather than a more conventional hollow cathode. While hollow cathodes are the standard for operational thrusters, they are complex to design and

fabricate, and require dedicated heating systems and careful gas management. For a laboratory-scale prototype, a simpler, lower-cost alternative was deemed appropriate. Following the approach demonstrated successfully by Lee [29], the cathode design uses tungsten filament sources derived from commercially available automotive light bulbs. Two 21 W bulbs will be stripped of their glass housings and repurposed as filament cathodes significantly reducing cost. Using two filaments in parallel is expected to provide a greater supply of electrons to the discharge than a single filament, improving ionisation efficiency while retaining the advantages of a simple, inexpensive source.

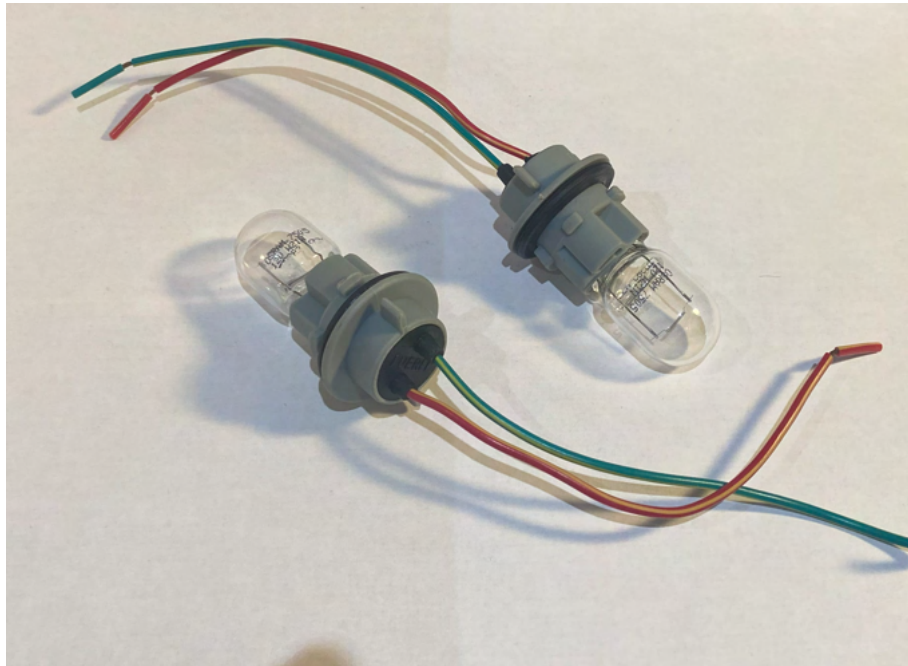


Figure 23: Prospective cathode elements: 21 W automotive bulbs and holders, to be repurposed as filament cathodes after removal of the glass housings.

The principal limitation of this approach is filament lifetime. Tungsten filaments are prone to evaporation and erosion when operated at high temperatures in plasma environments, and their useful operating life is typically much shorter than that of hollow cathodes. For this reason, the design is best suited to short-duration laboratory tests rather than extended campaigns. However, the simplicity and low cost of replacement filaments make this trade-off acceptable for this project.

At present, the CAD models do not include a finalised mounting solution for the cathode. The current plan is to design and 3D print a mount from PET-CF, similar to the thruster mount. The final design will be completed closer to the time of oper-

ation, once integration constraints with the vacuum facility are better understood.

3.4.5 Electrical System and Wiring

The electrical system of the thruster must supply stable power to three distinct loads: the discharge circuit, the electromagnet coils, and the cathode filaments. Each subsystem has different voltage and current requirements.

The discharge circuit is the primary high-voltage load, operating at approximately 300 V to accelerate ions within the channel. This supply must be stable and well-isolated, as fluctuations directly impact the thrust and specific impulse of the device. For this purpose, a Lambda GEN 300-2.5 programmable DC supply was selected, capable of delivering up to 300 V at 2.5 A. The supply includes programmable current limiting and remote control functionality, providing both protection during ignition and flexibility during experimental operation.

The electromagnet coils operate at comparatively low voltage but require continuous currents up to about 0.5 A. In this design, the inner and outer coils are supplied from the same channel of a RND 320-KA3305P dual-channel supply, wired in series so that they carry identical current. The inner coil is connected with reversed polarity relative to the outer coils, to establish the required radial field at the channel exit. Field strength is set by the supply current, while the relative weighting between inner and outer regions is fixed by the chosen turn counts and pole geometry. If fine adjustment is required, a small ballast resistor could be added to one branch to trim the balance.

The cathode filaments form a third electrical load. Each 21 W automotive bulb filament is rated for approximately 12 V and 1.75 A. Two filaments will be wired in parallel to increase the available electron emission. These are powered from the second channel of the RND 320-KA3305P supply, allowing independent control of cathode heating. A controlled current ramp during startup will be used to reduce thermal shock to the filaments and extend their operational life.

A key architectural choice in thruster power systems is whether to operate in a grounded or floating configuration. In a grounded configuration, the negative terminals of the discharge, coil, and cathode supplies are tied directly to the vacuum chamber wall, which is itself referenced to laboratory ground. This simplifies electrical layout, improves operator safety, and reduces the risk of uncontrolled potential differences between the thruster and chamber. The trade-off is that plasma

potentials are constrained by this ground reference, which can slightly reduce performance compared to floating operation. In floating mode, the thruster is electrically isolated from the chamber, allowing the plasma to establish its own potential relative to ground. This can sometimes reduce electron losses and improve efficiency, but requires more complex insulation and presents higher risks during laboratory testing [32].

For this project, a grounded configuration was selected. As a laboratory prototype, the primary goals are robustness, repeatability, and safe integration with the vacuum facility, rather than maximising absolute efficiency. Grounding also simplifies wiring and ensures that all supplies share a common, stable reference point, which reduces noise and prevents hazardous floating potentials.

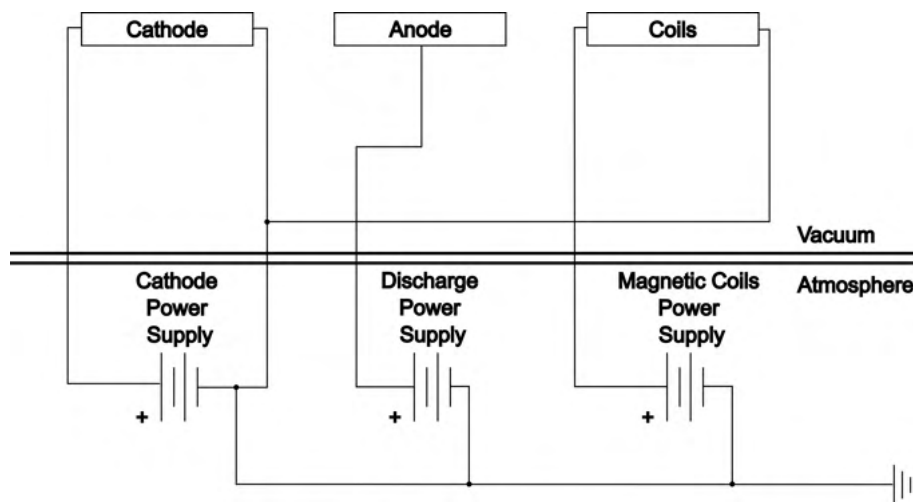


Figure 24: Simplified wiring schematic of the thruster showing independent supplies for the discharge circuit, electromagnet coils, and cathode filaments. All circuits share a common ground at the vacuum chamber, with HV and LV feedthroughs segregated.

A simplified wiring diagram is shown in Figure 24. Each supply is routed through a dedicated feedthrough, with high-voltage lines kept separate from the low-voltage coil and filament circuits to reduce cross-talk and hazard. Daisy-chained ground returns should be avoided in the actual implementation; instead, all supplies are tied individually to the chamber ground point. In operation, the startup sequence follows standard practice. First the cathode heater supply is energised, followed by the coils, and finally the discharge voltage is applied once emission is established.

4 Thruster Assembly

4.1 Coil Winder

Winding the electromagnet coils presented a significant manufacturing challenge. Each thruster configuration required multiple coils with several hundred turns (600 for the short configuration and 900 for the long), all of which needed to be wound under consistent tension to ensure reproducible resistance and packing density. Manual winding was ruled out as impractical, being both labour-intensive and prone to irregularities in turn spacing and tension. Commercial winding machines were investigated, but units capable of handling the required dimensions and turn counts were either prohibitively expensive or lacked the flexibility required for rapid prototyping. To overcome these constraints, a custom coil winder was designed and built in-house, combining low-cost 3D-printed components with stepper-motor actuation and Arduino-based control.

The winding process began with the steel coil cores, shown in Figure 25, which were cut, drilled, and tapped manually. These acted as the formers onto which the enamelled copper wire would be wound. Prior to winding, each core was wrapped in polyimide tape to provide electrical insulation and prevent the possibility of the coil shorting through the steel core during operation.



Figure 25: Steel coil cores prior to winding.

The overall winder assembly is shown in Figure 26. A drive stepper motor provided rotation through a 3D-printed chuck mounted on a bearing. Motion was transmitted using an elastic band running in a 3D-printed groove, with friction providing the coupling. The pulley diameters gave an effective 2:1 ratio, such that one motor revolution produced approximately two turns of the coil. The coil core was bolted through this driven chuck and supported at the free end by a second, freely rotating chuck of similar geometry to maintain alignment with minimal friction.

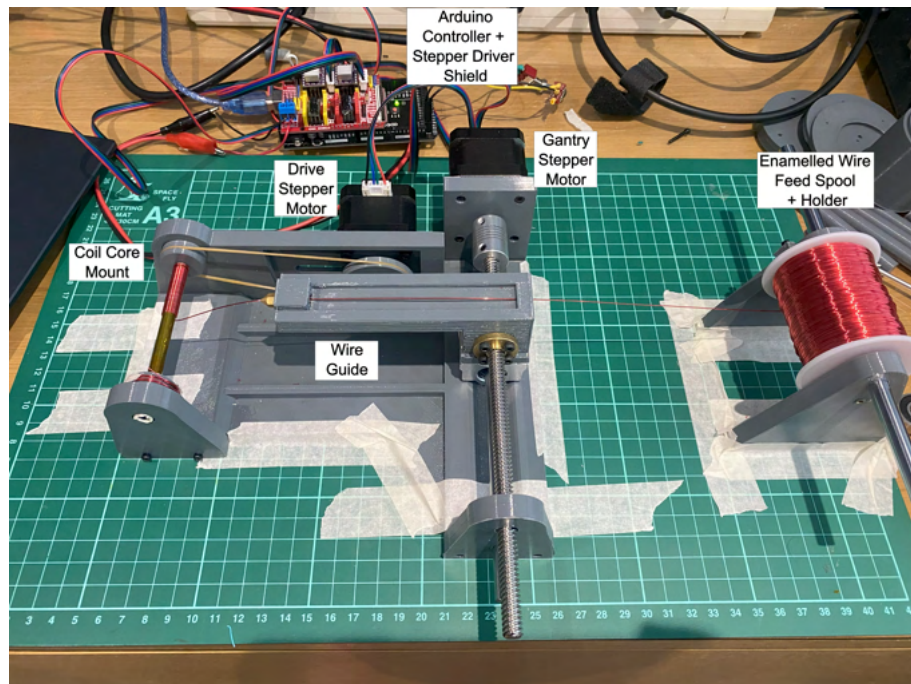


Figure 26: Custom-built coil winder with annotated components.

Wire guidance was achieved using a gantry that translated parallel to the coil axis, driven by a leadscrew and stepper motor. The wire passed through a 0.6 mm 3D printer nozzle mounted on the carriage. This nozzle size directly limited the maximum usable wire diameter, and therefore set the choice of magnet wire used in Chapter 3. During winding, the gantry traversed along the coil length to place turns side-by-side; on reaching the end of travel, it reversed to begin the next layer, building up the winding in a simple back-and-forth pattern.

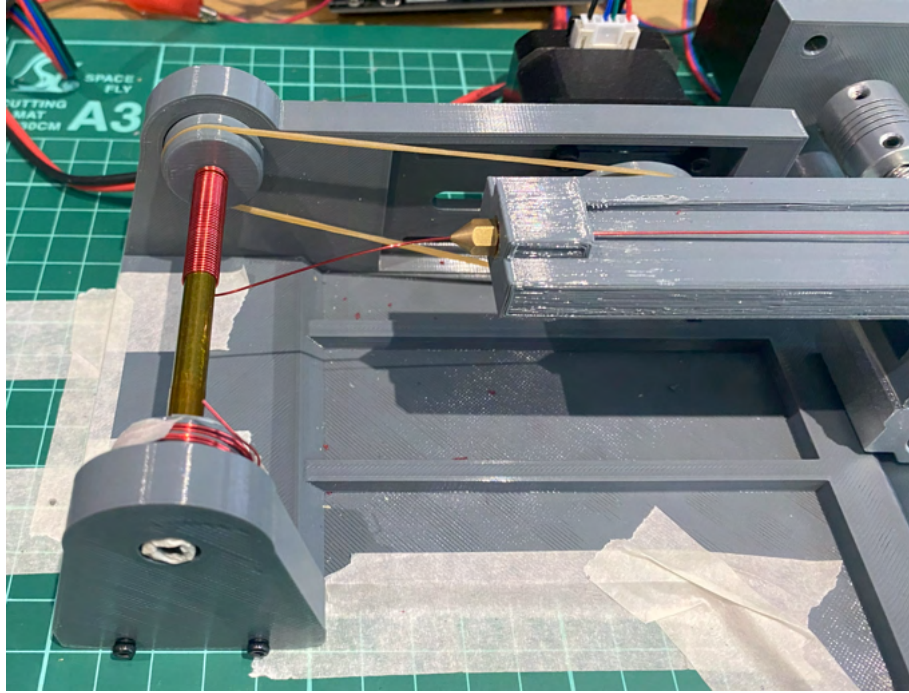


Figure 27: Close-up of the winding process showing wire guide and coil core.

Control of the two axes was handled by an Arduino microcontroller and driver shield. Both the rotation and traverse motions were executed on a clock-based control scheme rather than being indexed to absolute turn counts or carriage position. This approach kept the system inexpensive and relatively simple to program, while still allowing the production of tightly packed coils. A full version of the Arduino sketch used to operate the winder is included in Appendix B.4.

Figure 28 shows the completed sets of coils for the short and long thruster configurations. The consistency of these coils is assessed in the following subsection.



Figure 28: Completed short (right) and long (left) coils after winding and being wrapped in polyimide tape.

4.1.1 Coil Consistency

The electrical resistance of each coil was measured after winding to assess consistency, shown in Table 6. Resistance is directly related to the number of turns and packing density, so variation between nominally identical coils provides a useful indicator of manufacturing repeatability.

Short Coils	Resistance (Ω)	Long Coils	Resistance (Ω)
S1	0.57	L1	0.79
S2	0.54	L2	0.70
S3	0.59	L3	0.85
S4	0.59	L4	0.81
S5	0.60	L5	0.83

Table 6: Measured resistances of short and long coils used to assess winding consistency.

The consistency of each set of coils was quantified using the coefficient of variation (CV), defined as

$$CV = \frac{\sigma}{\mu} \times 100 \text{ (\%)} \quad (4.1)$$

where σ is the standard deviation of the coil resistances and μ is their mean. This normalised measure of spread allows for a direct comparison between the short and long coils.

The short coils exhibited a CV of 4.13%, while the long coils showed a higher CV of 7.30%. This indicates that the winder produced the short coils with reasonable consistency, but the longer coils suffered from greater variability.

The difference is likely attributable to limitations in the coil winding machine. In particular, uneven friction on the enamelled wire feed spool occasionally caused the wire to slip, introducing irregularities in tension and layer packing. Slippage of the drive belt is also a likely contributor, particularly for the longer coils where cumulative error across several hundred turns becomes more pronounced. In addition, the winder operates on a time-based turn count rather than an indexed turn-tracking system, which may introduce further error over extended winding runs. Overall, while the variability is noticeable, the measured resistances remain within acceptable bounds for laboratory operation.

Several potential improvements could be made to reduce this variability in future iterations of the coil winder. The most effective would be the introduction of an indexed turn counter or an optical encoder to directly synchronise coil rotation with gantry translation, eliminating reliance on time-based coordination. A positive-drive mechanism, such as a toothed belt or gear train, would also prevent slip at the chuck and ensure more consistent winding. An adjustable tensioning system for the feed spool would further stabilise friction on the wire, helping to maintain uniform packing density. Finally, the free-end support could be redesigned to be adjustable in length, as the current setup only accommodates the two coil sizes used in this project. Together, these refinements would significantly improve the repeatability, flexibility, and robustness of the winding process.

4.2 Boron Nitride Inserts

As mentioned in Chapter 3, the boron nitride discharge channel inserts were among the first components to be finalised, owing to their long manufacturing lead times and limited availability from specialist suppliers. Orders were placed early in the project to avoid delays to thruster assembly.

On receipt, the inserts were found to be accurate in dimension and within the specified tolerances, confirming the reliability of the supplier. The inserts are shown in

Figure 29. Some minor issues with localised edge rounding and small amounts of crumbling at sharp corners after a thruster test fit were observed, shown in Figure 30. These are consistent with the brittle nature of BN and are unlikely to affect performance. The affected areas were cosmetic rather than structural and no cracking was observed.

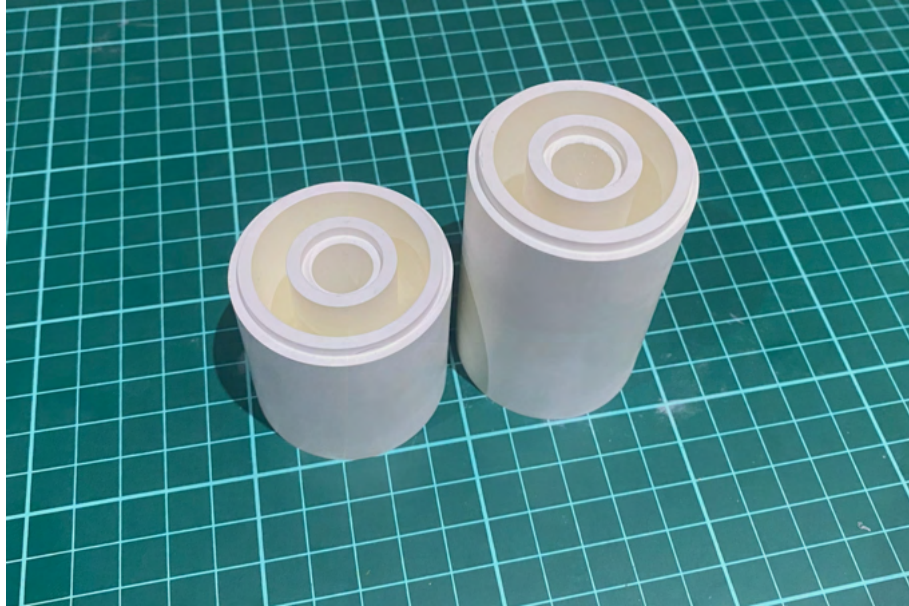


Figure 29: Boron nitride discharge channel inserts for the short (left) and long (right) thruster configurations, as received from the supplier.

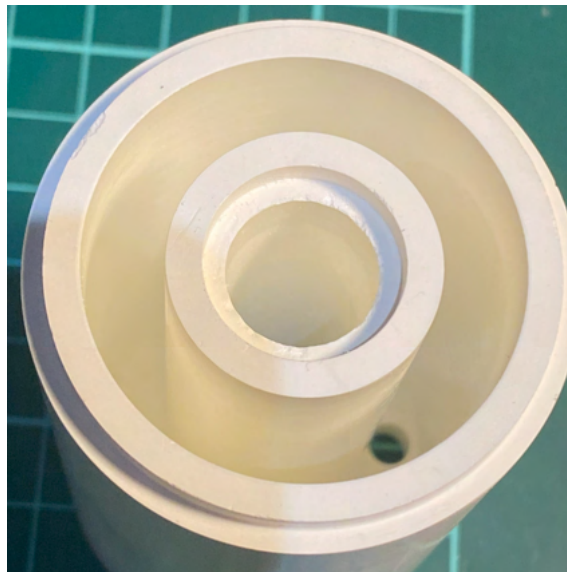


Figure 30: Close-up of the boron nitride insert showing minor edge rounding and localised crumbling at sharp corners after test fitting.

Overall, the components met the design requirements and were judged to be suitable for integration into the thruster.

4.3 Machined Parts

The steel components of the magnetic circuit (baseplate, pole pieces, and coil cores) were manufactured following completion of the CAD modelling described in Chapter 3. These parts were designed to be readily manufacturable from standard EN1A steel rod stock using straightforward machining operations, balancing material performance with cost and lead time.

Of these components, only the baseplate and outer pole were outsourced to an external supplier, as they required precision turning operations on equipment not available in-house. The coil cores and inner pole, by contrast, were produced manually using a combination of hand tools and finishing with sandpaper. This division of work reduced both cost and schedule risk while still ensuring the key magnetic circuit parts were manufactured within tolerance.

The coil cores were cut from a single 1 m length of 6 mm EN1A rod, then drilled and tapped to the required thread. Some difficulty was encountered in centring the pieces, but this was mitigated by deliberately oversized holes in the externally machined parts. The inner poles posed a greater challenge due to the bulk of material that had to be removed. The central hole is slightly offset, though this has not affected functionality. Surface finish was rougher than ideal, but time constraints prevented further refinement before this report.

The externally manufactured components also conformed closely to the CAD specifications. The machined features aligned well with the in-house parts, allowing straightforward assembly. On reflection, the surface finish could have been improved here as well, as some minor tool marks were visible, but these were cosmetic and have no effect on the functionality of the parts. Dimensional accuracy was within tolerance, and no distortion or warping was observed. Figure 31 shows the completed components prior to assembly.

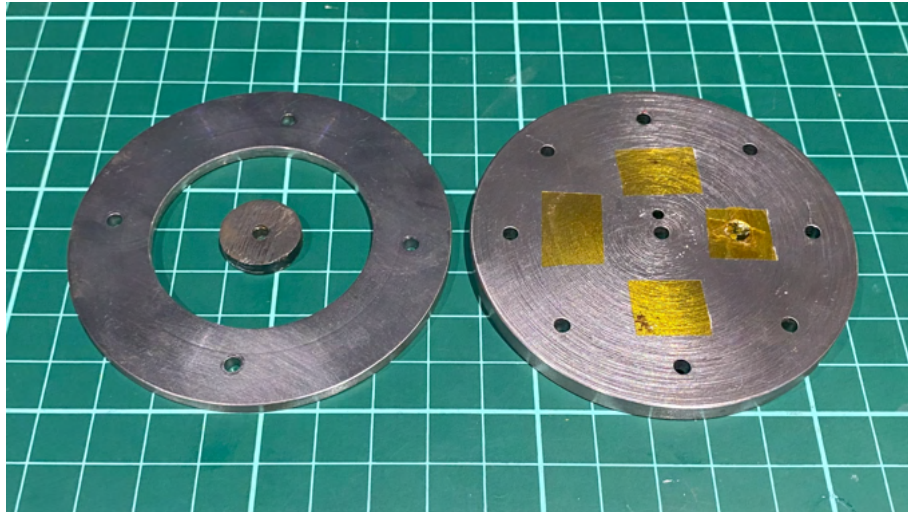


Figure 31: Machined EN1A steel components for the thruster magnetic circuit including the pole pieces (left) and the baseplate (right).

The combination of outsourced and in-house machining proved effective, ensuring that high-tolerance parts were delivered on schedule while allowing flexibility for iterative adjustments to simpler components. With the coils, boron nitride inserts, and the steel magnetic circuit parts complete, all major structural elements were available for integration into the full thruster assembly.

4.4 Thruster Assembly

The final stage was the integration of the manufactured components into a complete thruster assembly. Assembly followed the order established in the CAD models: the coils were mounted to the magnetic base mounted first, followed by installation of the boron nitride channel inserts. Finally the poles were attached locking the coils and inserts in place. The stainless steel anode would then be inserted through the front of the thruster.

Figures 32–34 show the assembly at various stages. Both short and long discharge channel configurations were completed successfully, validating the modular approach developed in Chapter 3.



Figure 32: Thruster during mid-assembly showing the coils and BN inserts installed on the magnetic base.

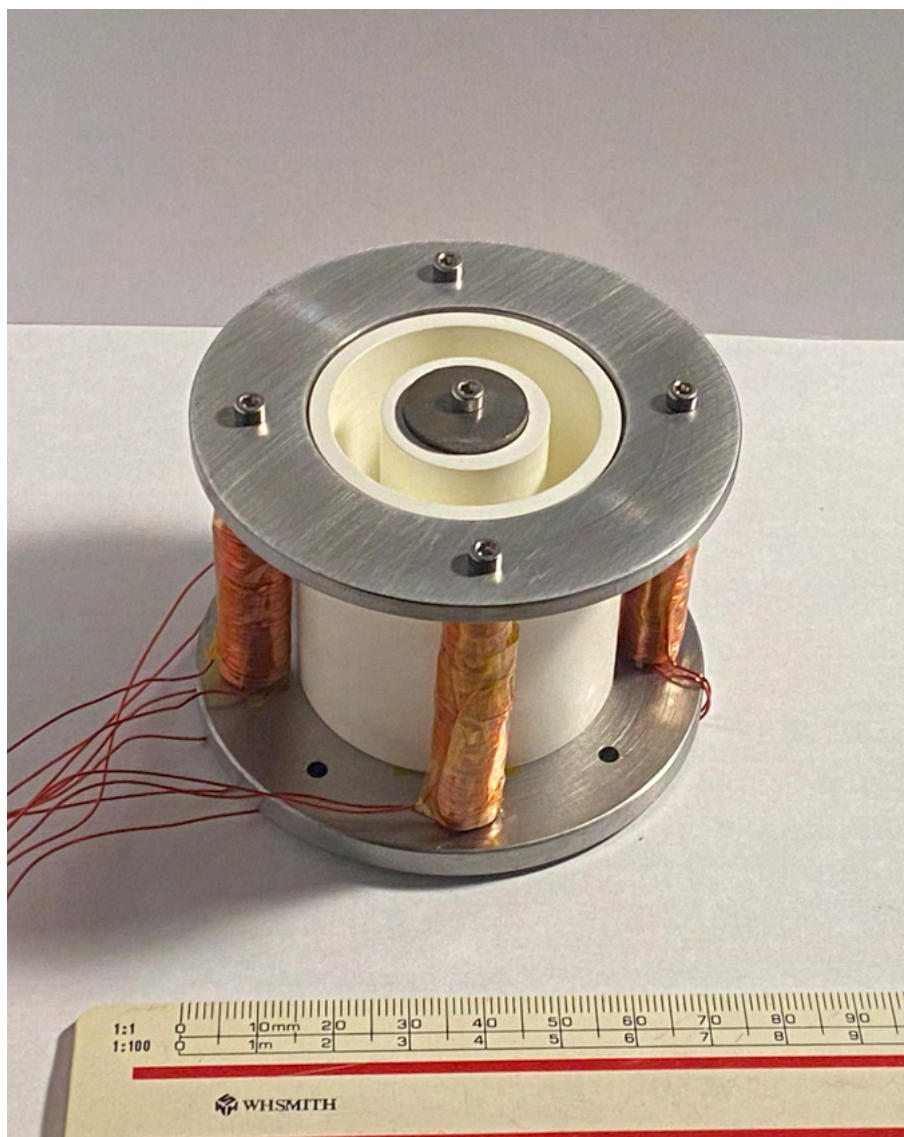


Figure 33: Completed thruster assembly in the short-channel configuration.

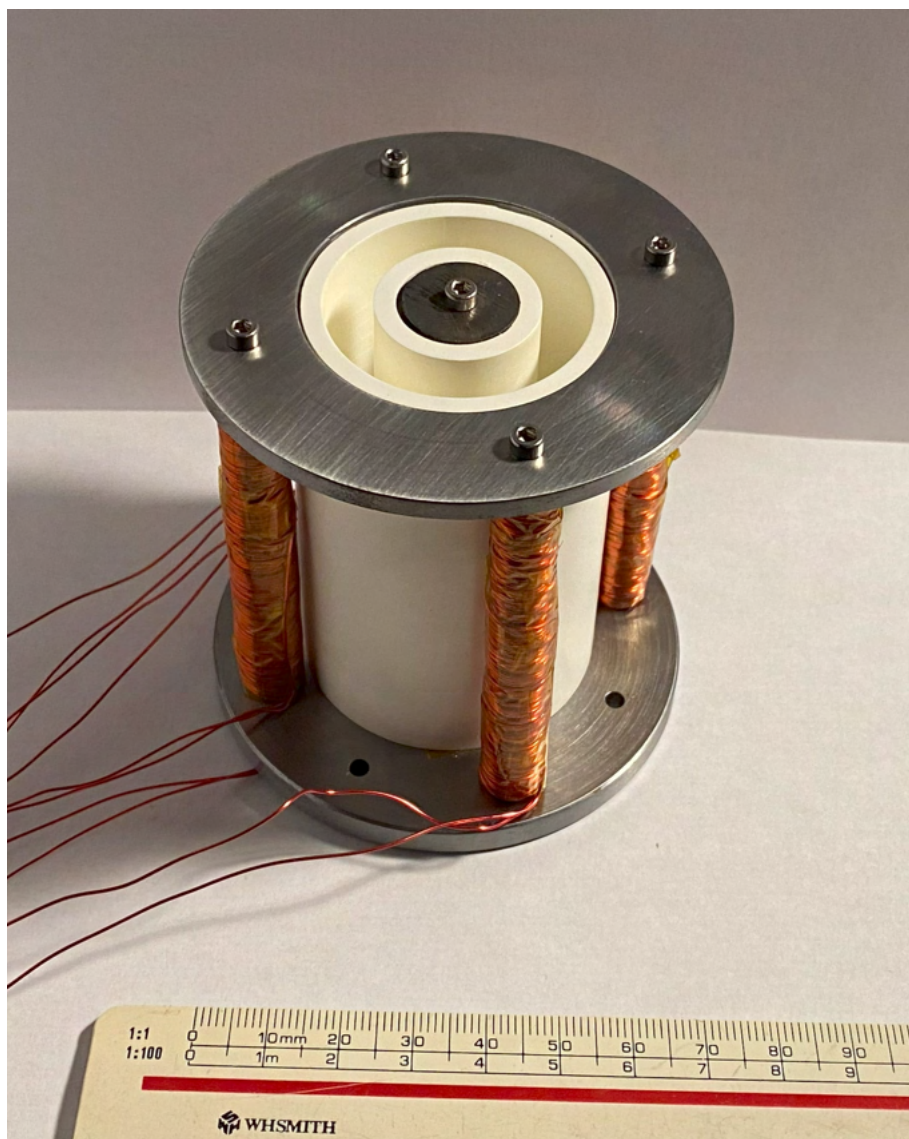


Figure 34: Completed thruster assembly in the long-channel configuration.

5 Conclusion

This project set out to design and realise a laboratory-scale Hall effect thruster operating on argon propellant. The work progressed from scaling analysis and magnetic circuit simulations through CAD modelling, material procurement, and physical assembly, with each stage shaped by the constraints of cost, manufacturability, and laboratory capability.

The resulting design meets its primary objectives. A five-coil magnetic circuit was developed and validated in simulation, demonstrating that both short and long channel configurations could sustain the required radial field distribution within the thermal limits of the coil. These analytical foundations were translated into hardware: boron nitride channel inserts were manufactured to specification, EN1A steel was adopted as a practical substitute for 1008, and a custom-built coil winder enabled consistent production of the electromagnet coils. Assembly of the thruster in both short- and long-channel forms confirmed that the CAD models were manufacturable and internally consistent.

Some compromises were necessary. A filament-based thermionic cathode was selected in place of a hollow cathode, trading lifetime and effectiveness for simplicity and cost. EN1A steel is expected to underperform slightly compared to 1008, though it should still achieve adequate performance for a non-flight thruster. The anode design has not yet been validated by fluid modelling. Nevertheless, the thruster is manufactured and ready for integrating into a test set up.

5.1 Cost Breakdown

One of the key objectives of this project was to design a thruster that could be replicated and adapted by other institutions. Since accessibility is closely tied to cost, a formal requirement was set to keep the hardware cost below £1000. Table 7 shows that the final thruster hardware cost was approximately £452, comfortably within this limit and demonstrating the design's viability for wider academic adoption.

Item	Cost (£)	Notes
Thruster		
Boron Nitride Inserts	161.72	
EN1A Machined Parts	180.02	Base Plate and Outer Pole
Coil Core Stock	3.90	6mm EN1A Rod Stock (1m)
Inner Pole	3.26	17mm EN1A rod Stock (25mm)
Coil Wire	31.03	24 AWG enamelled wire (500g)
Cathode	18.98	2x 21W bulbs + holder
Hook up Wire	29.28	20 AWG, 100m
Polyimide Tape	6.79	2x 33m rolls
Hardware	16.60	M2.5 Bolts (40 total)
Thruster Subtotal	451.58	
Propellant Feed System		
Mass Flow Controller	1709.40	Alicat 10 SCCM Full Flow
Argon Gas Bottle	96.59	2.36m3
Gas Bottle Regulator	36	Single Stage
Argon Line Adaptor	14.71	3/8 BSP to 4mm push fit
Ceramic Gas Break	64.50	
Swagelok Connectors	24.50	2x 4mm to 1/8"
Anode	11.79	304 Stainless Tube (4mm OD, 800mm)
PTFE Tape	1.79	12m
Connectors	12.78	M5 Male to 4mm Push fit
Feed System Subtotal	1972.06	262.66 (exc. MFC)
Power Supplies		
Discharge Power Supply	1515.28	Lambda Gen 300-2.5
2 Channel Bench Supply	249.31	RND 320-KD3305P
Power Supply Subtotal	1764.89	
Total Cost	4188.53*	

Table 7: Cost breakdown of the thruster and ancillary systems. *note this value excludes vacuum chamber costs

While the thruster hardware itself was delivered well under the £1000 requirement, Table 7 makes clear that the majority of project expenditure lies not in the thruster, but in the ancillary systems required to operate it. The thruster hardware itself accounts for only approximately 11% of the total cost. By contrast, the discharge power supply (£1515) and the mass flow controller (£1709) together represent more than 75% of the expenditure, even before considering the cost of a suitable vacuum chamber, which is not included in the breakdown but typically dominates

overall project budgets.

This distinction underlines a key point: while the thruster hardware can be manufactured cheaply and flexibly, meaningful operation is inseparable from access to expensive laboratory infrastructure. Items such as power supplies and mass flow controllers have relatively modest running costs once purchased, but vacuum facilities demand both a substantial initial investment and ongoing maintenance. As such, the most practical solution would be to increase collaboration between universities and industrial partners, enabling wider access to these facilities without duplicating infrastructure costs.

5.2 Future Work

The thruster developed in this project represents a manufacturable prototype, but its value as a research asset depends on further development and validation. It is anticipated that subsequent cohorts of MSc and PhD students at Cranfield will continue this work, progressively advancing the design into a more capable and versatile research platform.

The immediate priority is the completion of remaining hardware: final manufacture of the stainless steel anode, fabrication of cathode and thruster mounts, and integration of the assembled device into the vacuum chamber. These steps will allow the thruster to be commissioned alongside the propellant feed and power supply systems.

Once assembled, the first phase of testing should focus on achieving reliable ignition and steady-state discharge, with clear procedures developed to consistently achieve this. Verifying stable operation will provide confidence in the basic functionality of the design and establish baseline conditions for further characterisation.

The next stage should be systematic performance characterisation. This includes measuring discharge parameters, magnetic field behaviour, and thrust, with the aim of benchmarking experimental results against the predictions from the scaling laws and magnetic circuit simulations presented in this report. Validating plasma depth and ionisation efficiency against these models will be particularly important in confirming the design methodology.

In the longer term, the modular nature of the thruster (interchangeable channel lengths, replaceable anodes, and externally mounted cathodes) offers scope for

iterative research. Future students may explore refinements to the propellant distribution system, cathode coupling strategies, and discharge stability. Beyond incremental improvements, the thruster could serve as a platform for testing advanced concepts such as magnetic shielding or alternative propellants, thereby extending its research impact.

In summary, future work should proceed in three stages: complete integration and commissioning, establish and benchmark baseline performance, and iteratively expand the design into a flexible experimental platform. Through this staged progression, the device can evolve from a low-cost prototype into a valuable long-term research asset for Cranfield's electric propulsion programme.

5.3 Final Word

Beyond the technical outcomes, this project has demonstrated what can be achieved within the scope of a Master's thesis. All aims were met; the design was advanced from first principles through analysis and simulation to a manufacturable prototype, with critical components produced and the supporting systems identified. Whilst commissioning remains as future work, the results confirm that complex electric propulsion hardware can be realised systematically within the resources of a single student project.

Equally important is the project's alignment with the wider objective of developing technical expertise among UK graduates. The inherently multidisciplinary nature of Hall Effect Thruster design demanded the integration of physics, numerical modelling, electrical and mechanical engineering, cost management, and practical fabrication. In doing so, it fostered a breadth of technical and professional skills that reflect the requirements of the aerospace sector.

The success of this project should therefore serve as an example of what universities ought to encourage their students to achieve. Not only producing tangible hardware outcomes, but also cultivating the capabilities and confidence required to strengthen the UK's position in advanced propulsion research and industry. In this sense, the significance of the work extends beyond the thruster itself, demonstrating the educational and strategic value of projects that take students from concept to realisation.

References

- [1] Dan M. Goebel, Ira Katz, and Ioannis G. Mikellides. *Fundamentals of Electric Propulsion*. Ed. by Jon Hamkins. 2nd. John Wiley & Sons, Nov. 2023. ISBN: 978-1-394-16321-2.
- [2] E. Y. Choueiri. *A Critical History of Electric Propulsion: The First 50 Years (1906-1956)*. 2004. doi: 10.2514/1.9245.
- [3] V. A. Shchepetilov. "Development of Electrojet Engines at the Kurchatov Institute of Atomic Energy". In: *Physics of Atomic Nuclei* 81 (7 Dec. 2018), pp. 988–999. ISSN: 10637788. doi: 10.1134/S1063778818070104.
- [4] V. Kim et al. "History of the Hall Thrusters Development in USSR". In: *30th International Electric Propulsion Conference*. Sept. 2007.
- [5] V. ZHURIN, A. POROTNIKOV, and V. SHADOV. "Electric propulsion research and development in the USSR". In: *AIAA International Electric Propulsion Conference*. American Institute of Aeronautics and Astronautics (AIAA), Nov. 1976. doi: 10.2514/6.1976-1073.
- [6] Brian R. Frongello et al. "Spacecraft electric propulsion at an inflection point". In: *Accelerating Space Commerce, Exploration, and New Discovery conference, ASCEND 2021*. American Institute of Aeronautics and Astronautics Inc, AIAA, Nov. 2021. ISBN: 9781624106125. doi: 10.2514/6.2021-4151.
- [7] Dan Lev et al. *The technological and commercial expansion of electric propulsion*. June 2019. doi: 10.1016/j.actaastro.2019.03.058.
- [8] Archit Bapat, Pramod B. Salunkhe, and Aakash V. Patil. *Hall-Effect Thrusters for Deep-Space Missions: A Review*. Feb. 2022. doi: 10.1109/TPS.2022.3143032.
- [9] Thomas F Munro-O'brien and Charles N Ryan. "Performance Comparison Between Modular SPT and TAL Type Hall Thrusters Operating on Krypton". In: *38th International Electric Propulsion Conference*. June 2024. URL: <https://www.researchgate.net/publication/381619917>.
- [10] Noah Z. Warner and Manuel Martínez-Sánchez. "Design and preliminary testing of a miniaturized TAL Hall thruster". In: *Collection of Technical Papers - AIAA/ASME/SAE/ASEE 42nd Joint Propulsion Conference*. Vol. 8. 2006, pp. 6422–6435. ISBN: 1563478188. doi: 10.2514/6.2006-4994.
- [11] Busek. *BHT-600 Datasheet*. Tech. rep. Busek, Mar. 2021. URL: <https://www.busek.com/bht600>.
- [12] Busek. *BHT-200 Datasheet*. Tech. rep. Busek, 2021. URL: <https://www.busek.com/bht200>.
- [13] Kybeom Kwon, Mitchell L R Walker, and Dimitri N Mavris. "Study on Anomalous Electron Diffusion in the Hall Effect Thruster". In: *International Journal of Aeronautical & Space Science* 15 (3 2014), pp. 112–121. doi: 10.5139/IJASS.2014.15.3.23. URL: <http://ijass.orgp>ISSN:2093-274xeISSN:2093-2480.

- [14] Megan N Maikell. *Characterization and Anomalous Diffusion Analysis of a 100w Low Power Annular Hall Effect Thruster Low Power Annular Hall Effect Thruster*. Tech. rep. Air Force Institute of Technology, Mar. 2019. URL: <https://scholar.afit.edu/etd/2226>.
- [15] E. Ahedo, J. M. Gallardo, and M. Martínez-Sánchez. “Effects of the radial plasma-wall interaction on the Hall thruster discharge”. In: *Physics of Plasmas* 10 (8 Aug. 2003), pp. 3397–3409. ISSN: 1070664X. doi: 10.1063/1.1584432.
- [16] S. Yoshikawa and D. J. Rose. “Anomalous diffusion of a plasma across a magnetic field”. In: *Physics of Fluids* 5 (3 1962), pp. 334–340. ISSN: 10706631. doi: 10.1063/1.1706619.
- [17] David H. Manzella and John M. Sankovic. “Hall thruster ion beam characterization”. In: *31st Joint Propulsion Conference and Exhibit*. American Institute of Aeronautics and Astronautics Inc, AIAA, July 1995. doi: 10.2514/6.1995-2927.
- [18] Matthew Baird et al. “Plume divergence and discharge oscillations of an accessible low-power hall effect thruster”. In: *Applied Sciences* 11 (4 Feb. 2021), pp. 1–16. ISSN: 20763417. doi: 10.3390/app11041973.
- [19] Thomas Burton et al. “Plasma-induced erosion on ceramic wall structures in hall-effect thrusters”. In: *Journal of Propulsion and Power* 30 (3 July 2014), pp. 690–695. doi: 10.2514/1.B34882.
- [20] Ryan W. Conversano et al. “Development and initial testing of a magnetically shielded miniature hall thruster”. In: *IEEE Transactions on Plasma Science* 43 (1 Jan. 2015), pp. 103–117. ISSN: 00933813. doi: 10.1109/TPS.2014.2321107.
- [21] “Magnetic shielding of a laboratory Hall thruster. I. Theory and validation”. In: *Journal of Applied Physics* 115 (4 Jan. 2014). ISSN: 10897550. doi: 10.1063/1.4862313.
- [22] L. Garrigues et al. “Operation of a low-power Hall thruster: Comparison between magnetically unshielded and shielded configuration”. In: *Plasma Sources Science and Technology* 28 (3 Mar. 2019). ISSN: 13616595. doi: 10.1088/1361-6595/ab080d.
- [23] Hao Tian Fan et al. “Improving the hall thruster global efficiency over a wide flow-rate range”. In: *Journal of Propulsion and Power* 37 (4 2021), pp. 625–633. ISSN: 15333876. doi: 10.2514/1.B38208.
- [24] Busek. *BHT-100 Datasheet*. Tech. rep. Busek, Aug. 2021. URL: <https://www.busek.com/bht100-hall-thruster>.
- [25] Richard R. Hofer, Robert S. Jankovsky, and Alec D. Gallimore. “High-specific impulse Hall thrusters, part 1: Influence of current density and magnetic field”. In: *Journal of Propulsion and Power* 22 (4 Aug. 2006), pp. 721–731. ISSN: 15333876. doi: 10.2514/1.15952.
- [26] Ryan W. Conversano et al. “Performance Enhancement of a Long-Life, Low-Power Hall Thruster for Deep-Space Smallsats”. In: *2017 IEEE Aerospace Conference*. IEEE, Mar. 2017, p. 421. ISBN: 9781509016136. doi: 10.1109/AERO.2017.7943577.

- [27] P Hruby et al. "Overview of Busek Electric Propulsion". In: *36th International Electric Propulsion Conference*. Sept. 2019.
- [28] Eunkwang Lee et al. "Scaling approach for sub-kilowatt hall-effect thrusters". In: *Journal of Propulsion and Power* 35 (6 2019), pp. 1073–1079. ISSN: 15333876. doi: 10.2514/1.B37424.
- [29] Ty D. Lee. "A Small Modular Laboratory Hall Effect Thruster". Master's thesis. University of California, 2014.
- [30] Dan Lev et al. "The Development of CAM200-Low Power Hall Thruster". In: *Trans. JSASS Aerospace Tech. Japan* 14 (ists30 2016), pp. 217–223.
- [31] James H. Wetherbee et al. "Student Design and Analysis of a Hall Effect Thruster". In: *AIAA SciTech Forum and Exposition, 2023*. American Institute of Aeronautics and Astronautics Inc, AIAA, 2023. ISBN: 9781624106996. doi: 10.2514/6.2023-1598.
- [32] Ugur Kokal, Nazli Turan, and Murat Celik. "Experimental Investigation of the Electrical Wiring Configuration of the HK40 Hall Thruster Operation". In: *Journal of Aerospace Technology and Management* 15 (Feb. 2023). ISSN: 21759146. doi: 10.1590/jatm.v15.1316.

A Executive Summary: Development of a Low-Cost Stationary Plasma Thruster Testbed for Use in Educational and Research Applications

This project set out to design and manufacture a low-cost Stationary Plasma Thruster (SPT) testbed for use in research and educational applications at Cranfield University. Hall Effect Thrusters (HETs) are increasingly central to modern satellite propulsion, balancing high specific impulse with moderate thrust levels. Their role in large constellations and deep-space missions underlines the importance of developing UK expertise in their design and operation. By progressing from first principles through scaling analysis, simulation, detailed design, and fabrication, this work demonstrates both the technical feasibility of building such a device within the scope of a single Master's thesis, and the educational value of embedding students in the full engineering lifecycle.

Motivation and Objectives

Electric propulsion (EP) offers significant advantages over chemical propulsion by enabling higher exhaust velocities and reducing propellant mass. Among EP systems, Hall Effect Thrusters occupy a unique position, offering higher thrust than ion engines while retaining strong efficiency and lifetime characteristics. Their dominance in the commercial and institutional market makes them a strategically important technology.

The aims of this project were therefore threefold:

- To design and manufacture a modular, laboratory-scale SPT capable of operating on low-cost propellants, primarily argon;
- To create a platform for training and education, enabling students to gain hands-on experience in HET operation, diagnostics, and performance analysis;
- To provide a foundation for future research into alternative propellants and advanced thruster concepts such as magnetic shielding.

A key project requirement was affordability. The thruster hardware itself was required to be delivered for less than £1000, ensuring accessibility and replicability by other institutions.

Methodology

The design methodology combined theoretical analysis, empirical scaling laws, numerical modelling, and practical engineering. The process followed a clear progression:

1. **Scaling analysis:** Established baseline channel geometry, propellant mass flow, and predicted performance using empirical relations derived from other sub-kilowatt thrusters. These relations were adapted from xenon to argon propellant, balancing thrust and specific impulse trade-offs.
2. **Magnetic circuit design:** Developed a five-coil magnetic circuit (central coil plus four outer coils) using Ansys Maxwell finite element analysis. Both short (42 mm) and long (65 mm) discharge channel configurations were studied to compare plasma depth and thermal performance of the coils.
3. **CAD modelling:** Created a detailed 3D design in SolidWorks, specifying all components including boron nitride channel inserts, EN1A steel magnetic cores, stainless steel anode, coils, and mounting structures.
4. **Manufacture:** Fabricated and assembled the thruster using a mix of in-house machining, external suppliers, and custom tools. A bespoke Arduino-driven coil winder was developed to produce consistent electromagnet coils with several hundred turns each.
5. **Subsystems:** Designed ancillary systems for propellant feed (based on an Alicat mass flow controller, Swagelok fittings, and a ceramic electrical isolator), cathode integration (low-cost tungsten filaments repurposed from automotive bulbs), and electrical supply (300 V discharge circuit, coil supply, and independent cathode heating).

At each stage, design choices were informed by the dual constraints of physics (ensuring adequate electron confinement and ion acceleration) and manufacturability (material availability, cost, and workshop capability).

Results

The final thruster assembly was realised in both short- and long-channel configurations. The design meets its stated requirements:

- **Cost:** The thruster hardware was delivered for £452, well within the £1000 limit. The majority of project expenditure lay in ancillary systems, particularly the power supplies and mass flow controller.
- **Performance (predicted):** At 300 V discharge voltage and 0.175 mg/s argon mass flow, the thruster is predicted to deliver approximately 4.9 mN of thrust at a specific impulse of 2855 s.
- **Magnetic circuit:** Simulations confirmed that both configurations sustain the required radial field distribution. The long configuration provides a greater plasma depth (up to 47 mm at short-duration currents) and is less sensitive to coil thermal limits, though it may increase wall interactions.
- **Manufacturability:** All components were produced successfully, with boron nitride inserts and EN1A steel parts meeting tolerance requirements. The modular design allows interchangeable inserts, replaceable anodes, and flexible cathode positioning.

Although the thruster has not yet been commissioned, the manufacturable hardware represents a successful prototype ready for integration with Cranfield's vacuum facility.

Discussion

The project highlighted several key findings:

- **Feasibility of low-cost hardware:** The thruster itself can be built cheaply and reliably; infrastructure costs dominate project budgets. Collaboration between institutions will be essential to broaden access to expensive facilities such as vacuum chambers and high-precision diagnostics.
- **Design trade-offs:** Adopting argon reduces cost but reduces desired performance compared with xenon. Substituting EN1A steel for 1008 results in marginally lower magnetic performance but ensures availability and machinability in the UK supply chain. Tungsten filament cathodes simplify design but will require frequent replacement.
- **Educational value:** The project demonstrates the value of exposing students to the full engineering lifecycle from theoretical principles, through simulation and design, to physical realisation. Such projects cultivate multi-

disciplinary skills that align directly with industry needs.

Future Work

Further development should proceed in three phases:

1. **Commissioning:** Integrate the thruster with the propellant feed, power supply, and vacuum chamber. Establish repeatable ignition and steady-state operation.
2. **Characterisation:** Benchmark discharge behaviour, thrust, and efficiency against predictions. Validate scaling laws and magnetic circuit performance experimentally.
3. **Iteration:** Explore refinements such as improved anode distribution, cathode positioning, and eventual adoption of hollow cathodes. Longer-term research could investigate alternative propellants and magnetic shielding.

Conclusions

This project has met its aims, demonstrating that complex electric propulsion hardware can be realised systematically within the resources of a Master's thesis. The manufacturable SPT prototype provides a tangible foundation for both research and education, at a cost accessible to universities.

Equally significant is the contribution to graduate training. The multidisciplinary nature of the project required integration of physics, simulation, mechanical and electrical engineering, and practical manufacturing. It has therefore cultivated the technical expertise and confidence required of engineers entering the UK space sector.

The success of this work should serve as an example of the type of ambitious, hardware-focused projects that universities should promote. By enabling graduates to deliver real engineering outcomes, such projects strengthen both institutional capability and the UK's position in advanced propulsion research and industry.

B Appendix B

B.1 Scaling Law Dataset

Thruster	P	U_d	d	h	L	\dot{m}_p	T	I_{sp}
SPT-20	52.4	180	15	5	32	0.47	3.9	839
SPT-25	134	180	20	5	N/A	0.59	5.5	948
HET-100	174	300	23.5	5.5	14.5	0.5	6.8	1386
KHT-40	187	325	31	9	25.5	0.69	10.3	1519
KHT-50	193	250	42	8	25	0.88	11.6	1339
HEPS-200	195	250	42.5	8.5	25	8.8	11.2	1300
BHT-200	200	250	21	5.6	N/A	0.94	12.8	1390
KM-32	215	250	32	7	16	1	12.2	1244
SPT-50M	245	200	39	11	25	1.5	16	1088
SPT-30	258	250	24	6	11	0.98	13.2	1234
KM-37	283	292	37	9	17.5	1.15	18.5	1640
CAM200	304	275	43	12	N/A	1.09	17.3	1587
SPT-50	317	300	39	11	25	1.18	17.5	1746
A-3	324	300	47	13	30	1.18	18	1821
HEPS-500	482	300	49.5	15.5	25	1.67	25.9	1587
BHT-600	615	300	56	16	N/A	2.6	39.1	1530
SPT-70	660	300	56	14	25	2.56	40	1593
SPT-100	1350	300	85	15	25	5.14	81.6	1540

Table 8: Dataset of Hall Effect Thrusters primarily in the sub-kilowatt range used to establish the scaling law applied in this study. Columns list: P (input power, W), U_d (discharge voltage, V), d (mean channel diameter, mm), h (channel width, mm), L (channel length, mm), \dot{m}_p (propellant mass flow rate, mg/s), T (thrust, mN), and I_{sp} (specific impulse, s). [28]

B.2 SCCM Conversion Script - Matlab

```
1
2 close all; clear; clc;
3
4 % Convert SCCM to mg/s of various gases
5
6 SCCM = 1;
7
8 atoms_sec = SCCM * (6.02214179e23/(22.413996e3 * 60));
9
10 % Nitrogen
11 N2 = 28.014;
12 N2_mg = atoms_sec * 1.660539e-27 * N2 * 1e6;
13
14 % Argon
15 Ar = 39.948;
16 Ar_mg = atoms_sec * 1.660539e-27 * Ar * 1e6;
17
18 % Krypton
19 Kr = 83.798;
20 Kr_mg = atoms_sec * 1.660539e-27 * Kr * 1e6;
21
22 % Xenon
23 Xe = 131.293;
24 Xe_mg = atoms_sec * 1.660539e-27 * Xe * 1e6;
25
26 fprintf('SCCM to mg/s\n\nSCCM: %f\n\nNitrogen: %f mg/s\nArgon: %f mg/s\nKrypton: %f mg/s\nXenon: %f mg/s\n',SCCM,N2_mg,Ar_mg,Kr_mg,Xe_mg)
```

B.3 Larmor Radius - Matlab

```
1 close all; clear; clc;
2
3 B = 0.015; % T
4 Vb = 300; % V
5
6 m = 9.109e-31; % kg
7 M_Ar = 6.633e-26; % kg
8 M_Xe = 2.180e-25; % kg
9 M_N2 = 4.652e-26; % kg
10
11 e = 1.60e-19; % C
12
13 Tev = 25; % eV
14
15 re = (1/B * sqrt((8/pi) * (m/e) * Tev))*1000; % mm
16
17 ri_Ar = 1/B * sqrt(((2*M_Ar)/e)*Vb)*1000; % mm
18
19 ri_N2 = 1/B * sqrt(((2*M_N2)/e)*Vb)*1000; % mm
```

B.4 Coil Winder Arduino Sketch

```
1 #include <Wire.h>
2 #include <math.h>
3 #include <AccelStepper.h>
4 #include <Bounce2.h>
5
6 // Input Variables - Use to Tune
7 const int driveRPM = 150;
8 const int coilLength = 44; // mm
9 const float wireOffset = 0.55; // mm (Typically slightly more
    than wire diameter)
10 const int targetTurns = 300; // Keep Drive Ratio in mind (2:1
    currently)
11
12 // Hardware Parameters
13 const int stepsPerRev = 200;
14 const float screwPitch = 8; // mm/turn
15
16 // Pin Setup
17 const int startPin = 22;
18 const int dirPin = 23;
19 Bounce startDebounce = Bounce();
20 Bounce dirDebounce = Bounce();
21
22 const int driveStepPin = 2;
23 const int driveDirPin = 5;
24
25 const int lateralStepPin = 3;
26 const int lateralDirPin = 6;
27 const int lateralMStep1 = 43;
28 const int lateralMStep2 = 45;
29 const int lateralMStep3 = 47;
30
31 // Stepper Setup
32 AccelStepper driveStepper(AccelStepper::DRIVER, driveStepPin,
    driveDirPin);
33 AccelStepper lateralStepper(AccelStepper::DRIVER, lateralStepPin
    , lateralDirPin);
34
```

```

35 // Calculations
36 const float driveStepsPerSec = (driveRPM / 60.0) * stepsPerRev;
37 const float turnsPerLayer = ceil((float)coilLength / wireOffset)
    ;
38 const float lateralStepsPerSec = ((float)coilLength / screwPitch
    / turnsPerLayer) * driveStepsPerSec;
39
40 // Runtime counters
41 float driveStepCount = 0;
42 float lateralStepCount = 0;
43 float driveTurnsThisLayer = 0;
44 float driveTurnsAtLastReverse = 0;
45
46 // State Setup
47 int isRunning = 0;
48 int direction = 1;
49 int revFlag = 1;
50
51 unsigned long lastUpdate = 0;
52
53 void setup() {
54     // Stepper Setup
55     driveStepper.setMaxSpeed(1200);
56     driveStepper.setAcceleration(100);
57     driveStepper.setSpeed(driveStepsPerSec);
58
59     lateralStepper.setMaxSpeed(1200);
60     lateralStepper.setAcceleration(100);
61     lateralStepper.setSpeed(lateralStepsPerSec);
62
63     // Microstepping setup: full step mode
64     pinMode(lateralMStep1, OUTPUT);
65     pinMode(lateralMStep2, OUTPUT);
66     pinMode(lateralMStep3, OUTPUT);
67     digitalWrite(lateralMStep1, LOW);
68     digitalWrite(lateralMStep2, LOW);
69     digitalWrite(lateralMStep3, LOW);
70
71     // Switch Setup
72     pinMode(startPin, INPUT_PULLUP);

```

```

73     startDebounce.attach(startPin);
74     startDebounce.interval(25);
75
76     pinMode(dirPin, INPUT_PULLUP);
77     dirDebounce.attach(dirPin);
78     dirDebounce.interval(25);
79
80     // Driver Enable
81     pinMode(8, OUTPUT);
82     digitalWrite(8, LOW);
83
84     // Serial
85     Serial.begin(9600);
86     delay(1000);
87     Serial.println("Setup Complete");
88 }
89
90 void loop() {
91     startDebounce.update();
92     dirDebounce.update();
93     digitalWrite(8, LOW); // Enable driver
94
95     // Direction control
96     if (dirDebounce.fell()) {
97         direction = 1;
98         Serial.println("Direction: Forward");
99     }
100    if (dirDebounce.rose()) {
101        direction = -1;
102        Serial.println("Direction: Reverse");
103    }
104
105    // Start/Stop control
106    if (startDebounce.fell()) {
107        isRunning = 1;
108        lastUpdate = millis(); // Reset time tracking when starting
109        Serial.println("Start");
110    }
111    if (startDebounce.rose()) {
112        isRunning = 0;

```

```

113     driveStepper.setSpeed(0);
114     lateralStepper.setSpeed(0);
115     Serial.println("Stop");
116 }
117
118 // Set speed based on current direction + lateral reversal
119 driveStepper.setSpeed(direction * driveStepsPerSec);
120 lateralStepper.setSpeed(direction * revFlag *
    lateralStepsPerSec);
121
122 // Run motors continuously while running
123 if (isRunning) {
124     driveStepper.runSpeed();
125     lateralStepper.runSpeed();
126 }
127
128 // Time-based tracking block
129 unsigned long now = millis();
130 if (isRunning && (now - lastUpdate >= 250)) {
131     float elapsedSec = (now - lastUpdate) / 1000.0;
132
133     // Update step counts
134     driveStepCount += driveStepper.speed() * elapsedSec;
135     lateralStepCount += lateralStepper.speed() * elapsedSec *
        revFlag;
136
137     long driveTurns = driveStepCount / stepsPerRev;
138     long lateralTurns = lateralStepCount / stepsPerRev;
139     long driveTurnsThisLayer = driveTurns -
        driveTurnsAtLastReverse;
140
141     // Reverse lateral direction after one layer
142     if (driveTurnsThisLayer >= turnsPerLayer) {
143         driveTurnsAtLastReverse = driveTurns;
144         revFlag = -revFlag;
145         Serial.println("Layer complete - reversing lateral
            direction");
146     }
147
148     // Stop system at target

```

```

149     if (driveTurns >= targetTurns) {
150         isRunning = 0;
151         driveStepper.setSpeed(0);
152         lateralStepper.setSpeed(0);
153         Serial.println("Target reached - stopping all motion");
154     }
155
156     // Debug
157     Serial.print("Drive Turns: "); Serial.print(driveTurns);
158     Serial.print(" | Turns Remaining This Layer: "); Serial.
        print((turnsPerLayer - driveTurnsThisLayer));
159     Serial.print(" | Drive Speed: "); Serial.print(driveStepper.
        speed());
160     Serial.print(" | Lateral Speed: "); Serial.println(
        lateralStepper.speed());
161
162     lastUpdate = now;
163 }
164 }

```




18 April 2025

Dear Mr Worwood ,

Reference: CURES/24859/2025

Project ID: 28128

Title: Design of a Modular Hall Effect Thruster

We are pleased to inform you that you have successfully declared that your research project is a **Literature Review – based solely on openly available literature which is in the public domain, and you are undertaking desk-based research not involving any other form of data or information.**

You have also confirmed that your project **does not meet** any of the literature review specified exceptions, listed both within the relevant section of the CURES form and below:

1) Your supervisor has requested that you apply for approval through CURES because:

- The journals or data are in a sensitive area (please discuss this with your supervisor)
- The project will be embargoed **i.e. will not be publicly available via the Cranfield library immediately or longer term**

2) Approval is/will be specifically required by another external body e.g. journal publishers

Therefore, **you do not require ethical approval** and your CURES application will be automatically closed.

Please keep a copy of this letter safe, if this exception is in relation to your thesis project, you will need to include a copy with your final thesis submission.

If you have any queries, please contact CURES Support.

We wish you every success with your project.

Regards,

CURES Team